RESEARCH ARTICLE | AUGUST 22 2023

The loading on a vertical cylinder in steep and breaking waves on sheared currents using smoothed particle hydrodynamics

Special Collection: Recent Advances in Marine Hydrodynamics

Yong Yang (杨勇) ; Peter K. Stansby ; Benedict D. Rogers ; Eugeny Buldakov ; Dimitris Stagonas ; Samuel Draycott

Physics of Fluids 35, 087132 (2023)
https://doi.org/10.1063/5.0160021

Physics of Fluids ARTICLE pubs.aip.org/aip/pof

The loading on a vertical cylinder in steep and breaking waves on sheared currents using smoothed particle hydrodynamics

Cite as: Phys. Fluids **35**, 087132 (2023); doi: 10.1063/5.0160021
Submitted: 29 May 2023 · Accepted: 1 August 2023 ·
Published Online: 22 August 2023

Yong Yang (杨勇),[1,a)] Peter K. Stansby,[1] Benedict D. Rogers,[1] Eugeny Buldakov,[2] Dimitris Stagonas,[3] and Samuel Draycott[1]

AFFILIATIONS

[1]School of Engineering, University of Manchester, Oxford Road, Manchester M13 9PL, United Kingdom
[2]Department of Civil, Environmental and Geomatic Engineering, University College London, Gower Street, London WC1E 6BT, United Kingdom
[3]Department of Civil and Environmental Engineering, University of Cyprus, 1 Panepistimiou Avenue, P.O. Box 20537, 1678 Nicosia, Cyprus

Note: This paper is part of the special topic, Recent Advances in Marine Hydrodynamics.
[a)]**Author to whom correspondence should be addressed:** yong.yang-3@postgrad.manchester.ac.uk

ABSTRACT

Waves and currents coexist in a wide range of natural locations for the deployment of offshore structures and devices. This combined wave–current environment largely determines the loading of vertical surface piercing cylinders, which are the foundations typically used for offshore wind turbines along with many other offshore structures. The smoothed particle hydrodynamics (SPH) code DualSPHysics is used to simulate focused waves on sheared currents and assess subsequent loading on a vertical cylinder. Outputs from another numerical model are used to define the SPH inlet–outlet boundary conditions to generate the wave–current combinations. A modified damping zone is used to damp the waves, but allow the currents to exit the domain. Numerical results are validated against experimental measurements for surface elevation and associated loading on the cylinder. Four phase repeats are used in the SPH model to understand the harmonic structure of the surface elevation at the front face of the cylinder and associated loading. It is shown that the SPH model provides agreement with experimental measurements of harmonic components for both force and elevations. Taking advantage of the SPH method, wave amplitudes were increased up to, and beyond, the breaking threshold highlighting a complex relationship between peak force and wave phase, requiring detailed investigation. The numerical modeling of interactions of steep and breaking waves on sheared currents with the cylinder demonstrates the SPH model's capability for modeling highly nonlinear fluid–structure interaction problems.

I. INTRODUCTION

Combined wave–current fields exist in a wide range of nearshore and coastal regions suitable for the deployment of offshore renewable energy (ORE) systems. Wave characteristics, such as the wavelength, wave-induced velocities, and wave heights, are modified in the presence of a current,[1–3] which results in complex wave–current conditions that determine the loads on offshore systems. Focused waves are often selected as representative for reproducing extreme wave conditions to investigate extreme loads on offshore systems. Meanwhile, a current with a non-zero vorticity is more realistic in coastal regions, and a vertical cylinder is widely used as the substructure of typical offshore fixed wind turbines, which are mainly arranged in nearshore and coastal regions. Thus, prediction of loads acting on a vertical cylinder in combined focused waves and sheared currents conditions is of great significance for practical applications.

Interactions of waves and currents with a cylinder have been studied analytically, numerically, and experimentally. Key findings from studies are focused on the wave–current interaction process, load coefficients (drag and inertia), and structural loadings in combined wave–current conditions. The study of Lin and Li[4] for a bottom-mounted vertical square cylinder subject to combined wave–current loading indicated that the strength and frequency of vortex shedding

caused by the uniform current can be reduced in the presence of waves owing to nonlinear wave–current interaction. It is also shown that the vortex shedding plays an important role in the prediction of in-line force. Jian *et al.*[5] demonstrated that the water run-up on a bottom-mounted vertical circular cylinder becomes higher with an increase in the current speed and the total wave loads acting on the cylinder in combined short-crested wave–current conditions are larger compared with the wave loads in pure short-crested wave conditions. Li and Lin[6] found that the drag coefficients for a stationary submerged horizontal circular cylinder are affected significantly by currents, while the vertical inertia coefficients in combined wave–current conditions are similar to those in pure waves. It is demonstrated that a linear sum of the wave-induced force and the current-induced force cannot predict the actual force on the cylinder accurately in combined solitary wave–current conditions for a horizontal cylinder near the free surface in Ref. 7 and for a vertical cylinder mounted into the flume in Ref. 8. Studies concentrated on interactions of waves and currents with other types of structures, such as the truss model,[9] the jacket model,[10] the tidal turbine model,[11] the submerged plate,[12] and the jack-up platform,[13] also indicated the non-negligible effect of wave–current interactions on the loading compared to pure wave conditions or pure current conditions. It can be seen that the wave–structure interaction will be affected by the presence of a current, and the wave-induced force and current-induced force cannot be considered separately for the prediction of the actual force.

Harmonics of wave loads and surface elevations for structure in waves and in combined wave–current conditions were also investigated in previous studies. Fitzgerald *et al.*[14] presented a general phase-based harmonic separation method for fully nonlinear free-surface elevation and hydrodynamic force on a fixed structure, which uses time histories obtained from focused wave groups with phase shifts of 0°, 90°, 180°, and 270° interacting with the cylinder, respectively. Mohseni *et al.*[15] studied wave–cylinder interaction using mesh-based Computational Fluid Dynamics (CFD) with investigation on harmonics in wave run-up. It was found that wave run-up associated with high harmonics is involved in the scattered wave field around the fixed vertical cylinder for both short and long wave conditions. Chen *et al.*[16] studied the interactions of focused waves and sheared currents with a vertical surface piercing cylinder using mesh-based CFD. Two approaches for numerical modeling (the direct method and the coupling method) were used with the application of an iterative wave focusing methodology to achieve wave focusing at the location of the vertical cylinder in the presence of sheared currents. It is demonstrated that the four-phase based decomposition method can be used to obtain the harmonic structure of forces acting on a cylinder in combined waves and sheared currents accurately. Feng *et al.*[17] investigated the higher harmonic wave loads and moments on a bottom-mounted vertical cylinder using the four-phase based decomposition method, where it was found that the discrepancy between experimental results and numerical results existed in the third-order harmonic. Ghadirian *et al.*[18] studied the effects of wave–current interactions on wave forces on a vertical cylinder. Based on the four-phase based decomposition method on the experimental measurements, it was found that the surface elevation time histories of waves on the opposing current are the most nonlinear, while the surface elevation time histories of waves on the following current and the inline force time histories of waves with no current are the most linear. Jiang *et al.*[19] studied the nonlinear resonant behavior induced by higher-order harmonics for two boxes in a side-by-side arrangement. It was found that the second-order and third-order harmonic-induced wave resonances affect the horizontal wave forces on the boxes in this arrangement. Mj *et al.*[20] investigated the harmonic structure of wave-induced forces on a vertical cylinder for a range of unidirectional and directionally spread random sea-states, and a key finding showed that the harmonic coefficients are almost identical if fitted as powers of the linear inline force and its Hilbert transform for spread and unidirectional seas. Chen *et al.*[21] investigated the harmonic structure of hydrodynamic forces on a fixed ship-shaped floating production, storage, and offloading (FPSO) vessel hull, where it was found that the harmonic structure of the force is weakly dependent on the wave steepness and the FPSO bow diameter, while the higher-order harmonics increase rapidly with the decrease in the FPSO length.

Smoothed particle hydrodynamics (SPH),[22,23] as a Lagrangian and meshless technique for CFD, is ideally suited to solve fluid problems involving highly nonlinear deformation.[24–29] For numerical modeling of wave–current interaction, regular waves interacting with steady currents were studied in Ref. 30 using a circulating current system and in Ref. 31 using a non-reflective open boundary condition. Numerical modeling of focused waves on variable sheared currents was presented in Ref. 32 using open boundaries and a modified damping zone. The combination of open boundaries and a modified damping zone is also implemented in the present study. For interactions of waves and currents with a structure using the SPH method, they are rare compared with those using mesh-based CFD methods and experiments. Using a circulating current system based on the SPH method, Shi *et al.*[33] and Liu *et al.*[34] investigated the hydrodynamic response of a flexible floating boom and silt curtain under combined wave–current conditions, respectively. However, for considering loading on the structure in offshore and ocean engineering based on the SPH method, most previous studies concentrated on waves only without the presence of a current. Wen *et al.*[35] investigated the regular wave interacting with a vertical cylinder using weakly compressible SPH (WCSPH). Lind *et al.*[36] studied wave forces on a vertical cylinder including regular wave loading and focused wave loading using incompressible SPH (ISPH). Chow *et al.*[37] developed a numerical wave basin that is capable of simulating focused breaking waves interacting with a vertical cylinder using ISPH. However, a current is known to affect wave characteristics and thus wave loading. Therefore, one of the main scopes of this paper is modeling complex and extreme events of combined waves and sheared currents interacting with a vertical cylinder using the SPH method which is ideally suited to highly nonlinear problems, and this study has received no attention to date using the SPH method. The second scope is using the four-phase based harmonic separation method to validate the model's ability at capturing the harmonic structure of the elevations and loading.

The solver used in the present study is DualSPHysics which is an open-source SPH code accelerated on a graphics processing unit (GPU).[38] Numerical modeling of waves within DualSPHysics was presented in Ref. 39 using a wavemaker and a damping zone and in Ref. 40 using open boundaries. The two methods are well tested within DualSPHysics. The detailed implementation of open boundaries in DualSPHysics was given in Ref. 41. A numerical wave–current flume for waves on variable sheared currents was developed based on the combination of open boundaries and a modified damping zone acting on the vertical velocity component within DualSPHysics in Ref. 32.

Focused waves interacting with various sheared currents were validated with analytical linear solutions. Capasso *et al.*[42] have presented a similar combined use of a damping zone with inlet–outlet boundary conditions for simulating a moored wave buoy in waves and currents in DualSPHysics using a third-order reconstruction the wave profile and velocity field at the boundaries.

Various methods are used to achieve the focusing of waves at the specified point in space and time. Linear wave theory is used to calculate the initial phase of each wave component at the inlet to achieve a wave group focusing at a particular location and time.[43] An iterative wave generation approach is used to calculate the corrected phases for the wave generator input until all the wave components come into phase at the focal location as used in Ref. 44, and this approach was modified to include the dispersion relation considering waves in the presence of a current with a constant shear in Ref. 45. The iterative wave generation approach was extended to include both the phase correction and the amplitude correction in Ref. 46, and this type of iterative method was applied in Ref. 47 to generate waves over complex bathymetry, in Ref. 48 to generate waves on sheared currents, and in Ref. 11 to generate waves in the presence of very fast currents (0.8 m/s of following current). An improved iterative focusing methodology considering a linearized amplitude spectrum instead of a full nonlinear spectrum was presented in Ref. 49, and wave records at different positions are used for phase and amplitude iterations. This iterative wave focusing methodology was applied in experiments for the generation of focused waves on sheared currents[50] and in the numerical modeling for the generation of breaking focused waves.[51]

In this paper, interactions of focused waves and sheared currents with a vertical cylinder are investigated. The problem addressed is inertia dominated with limited effect of diffraction. The time histories of the surface elevation and flow kinematics used as boundary conditions at the inlet of the SPH wave–current flume are pre-computed using another Lagrangian numerical model,[52,53] hereby referred to as the Buldakov *et al.* model. An iterative wave focusing methodology[49] was used within the model to replicate the experiments. This approach was referred to as the coupling method by using the outputs of the Buldakov *et al.* model as the inputs of the mesh-based CFD model in Ref. 16. Compared with the direct method in Ref. 16 using the iterative wave focusing methodology in the 2D mesh-based CFD model, the coupling method has a higher computational efficiency. This is due to the application of the iterative wave focusing methodology in the faster Buldakov *et al.* model to calculate the required boundary conditions that a smaller 3D computational domain of the mesh-based CFD model can be used for wave-current-structure interactions. In this paper, the numerical results from the SPH model are initially estimated with the Buldakov *et al.* model for surface elevations and horizontal velocity profile without a cylinder in place to validate the accuracy of the generated wave–current conditions. Then, the numerical results from the SPH model are validated with experimental measurements of surface elevations and horizontal forces on the vertical cylinder. Four phase repeats are used to understand the harmonic structure of the surface elevation and associated loading. A convergence study for the horizontal force on the cylinder in focused wave condition and combined focused waves-sheared current conditions is presented. Finally, wave amplitudes are increased up to, and beyond, the breaking threshold, to model steep and breaking waves on sheared currents interacting with the vertical cylinder.

This paper is organized as follows: in Sec. II, the SPH model is outlined. In Sec. III, the experimental setup, the numerical setup, and the harmonic separation method are presented. In Sec. IV, the results of numerical modeling are compared with the experimental measurements including surface elevations, cylinder loading and harmonic components for model validation. In Sec. V, the numerical modeling of extreme wave–current conditions interacting with the vertical cylinder is presented. In Sec. VI, the conclusions and future work are given.

II. SMOOTHED PARTICLE HYDRODYNAMICS MODEL

The solver used for modeling wave-current-structure interactions in the present study is the SPH-based DualSPHysics code.[38] In SPH, a function f at position $\mathbf{r}$ can be estimated by the integral approximation as

$$f(\mathbf{r}) = \int_{\Omega} f(\mathbf{r}')W(\mathbf{r}-\mathbf{r}', h)\mathrm{d}\mathbf{r}', \tag{1}$$

where the integral is over the domain Ω, $W(\mathbf{r}-\mathbf{r}', h)$ is the kernel function, and h is the smoothing length. In the discrete domain, Eq. (1) can be approximated with a summation

$$f(\mathbf{r}_a) \approx \sum_b f(\mathbf{r}_b)\frac{m_b}{\rho_b}W(\mathbf{r}_a-\mathbf{r}_b, h), \tag{2}$$

where m_b/ρ_b is the volume of particle b, m_b is the particle mass, ρ_b is the particle density, and $W(\mathbf{r}_a-\mathbf{r}_b, h)$ is the kernel function between particle a and particle b. Note herein $f(\mathbf{r}_b)$ is written as f_b.

A. SPH governing equations

The continuity and momentum equations in the Lagrangian form can be written as

$$\frac{\mathrm{d}\rho}{\mathrm{d}t} = -\rho\nabla\cdot\mathbf{v}, \tag{3}$$

$$\frac{\mathrm{d}\mathbf{v}}{\mathrm{d}t} = -\frac{1}{\rho}\nabla P + \mathbf{g} + \mathbf{\Gamma}, \tag{4}$$

where ρ is the density, $\mathbf{v}$ is the velocity, t is the time, P is the pressure, $\mathbf{g}$ is the gravitational acceleration, and $\mathbf{\Gamma}$ refers to dissipative terms. In the SPH form, Eq. (3) including the density diffusion term can be written as

$$\frac{\mathrm{d}\rho_a}{\mathrm{d}t} = \rho_a\sum_b\frac{m_b}{\rho_b}\mathbf{v}_{ab}\cdot\nabla_a W_{ab} + \delta h c_a\sum_b\frac{m_b}{\rho_b}\mathbf{\Psi}_{ab}\cdot\nabla_a W_{ab}, \tag{5}$$

where m is the mass, W is the kernel function, h is the smoothing length, c is the speed of sound, and δ is the free parameter. The value of δ is set to 0.1 according to Antuono *et al.*[54] The density diffusion function $\mathbf{\Psi}_{ab}$ applied in the present study to avoid unphysical fluctuations in the pressure field is that of Fourtakas *et al.*[55] and is given by

$$\mathbf{\Psi}_{ab} = 2\left(\rho_{ba}^T - \rho_{ab}^H\right)\frac{\mathbf{r}_{ab}}{|\mathbf{r}_{ab}|^2}, \tag{6}$$

where superscripts T and H denote the total and hydrostatic component, respectively. In the SPH form, Eq. (4) can be written as

$$\frac{\mathrm{d}\mathbf{v}_a}{\mathrm{d}t} = -\sum_b m_b\left(\frac{P_b+P_a}{\rho_b\rho_a} + \Pi_{ab}\right)\nabla_a W_{ab} + \mathbf{g}. \tag{7}$$

The artificial viscosity[56] is a common stabilizing method in SPH. The viscosity term Π_{ab} applied in the present study is given by

$$\Pi_{ab} = \begin{cases} \dfrac{-\alpha \overline{c_{ab}} \mu_{ab}}{\overline{\rho_{ab}}} \mathbf{v}_{ab} \cdot \mathbf{r}_{ab} < 0 \\ 0 \ \mathbf{v}_{ab} \cdot \mathbf{r}_{ab} \geq 0 \end{cases}, \tag{8}$$

where $\overline{c_{ab}} = (c_a + c_b)/2$ is the mean speed of sound, $\overline{\rho_{ab}} = (\rho_a + \rho_b)/2$, $\mu_{ab} = h\mathbf{v}_{ab} \cdot \mathbf{r}_{ab}/(r_{ab}^2 + 0.01h^2)$ and α is the coefficient to provide stabilizing dissipation. The value of α is set to 0.001 in the present study to provide a slight dissipation. The kernel function W used in the present study is the quintic Wendland kernel[57] given by

$$W(r,h) = \alpha_D \left(1 - \frac{q}{2}\right)^4 (2q+1) \quad 0 \leq q \leq 2, \tag{9}$$

where α_D equals $7/(4\pi h^2)$ in 2D and $21/(16\pi h^3)$ in 3-D, and $q = r/h$ is the non-dimensional distance between particles, where r is the distance between particle a and particle b. The smoothing length is set equal to $h = 1.5 \times \sqrt{3} \times d_p$ in the present study with d_p the initial interparticle distance. An equation of state is used to determine the fluid pressure based on the particle density in WCSPH. The relationship between pressure and density in the present study is given by the following Morris' equation of state:

$$P = c_0^2(\rho - \rho_0), \tag{10}$$

where ρ_0 is the reference density which equals 1000 kg/m^3, and c_0 is the speed of sound at the reference density. The speed of sound at 60 m/s is used in the present study. Equation (10) is also used in Refs. 58 and 59 to reduce noise in the pressure field. Particle positions are updated as follows:

$$\frac{d\mathbf{r}_a}{dt} = \mathbf{v}_a, \tag{11}$$

where $\mathbf{r}$ is the position. Time stepping is given by the symplectic method with time step criterion given a Courant–Friedrichs–Lewy (CFL) value of 0.5 in the present study.

B. Boundary conditions

Open boundary conditions are implemented based on the buffer zones that the physical quantities, such as velocity, density, and surface elevation, can be imposed on the buffer particles or extrapolated from the fluid domain. The detailed implementation can be found in Ref. 41. The imposed physical quantities can be from theoretical solutions, experiments, and other numerical tools. The physical quantities extrapolated from the fluid domain are based on the use of ghost nodes. The open boundary conditions are applied in the present study for the generation of wave-alone and wave–current conditions and for particles to leave or enter the fluid domain.

The dynamic boundary condition (DBC)[60] is the default boundary treatment within DualSPHysics. Modified dynamic boundary conditions (mDBC) were introduced in detail in Ref. 61 such that the unphysical gap between fluid and boundary commonly observed with DBC can be avoided. The boundary particles are arranged in the same way as in DBC. The density of each solid particle is obtained from the position of related ghost node within the fluid domain using a linear extrapolation. In mDBC, a no-slip boundary condition is approximated with zero velocity applied to the boundary particles and is applied in the present study.

Periodic boundary conditions (PBCs) can be used to describe an infinitely long domain by using a periodically repeating finite domain within DualSPHyics.[38] To achieve this, particles located within nh ($n = 2$ in the present study) near an open lateral boundary on each lateral side of the domain are allowed to interact with the fluid particles of the opposite open lateral boundary on the other side of the domain completing the truncated support in a cyclic manner. The PBC is applied in the present study instead of solid side walls for the numerical wave–current flume. The general sketch of boundary conditions used in the numerical modeling of wave–current–structure interaction in the present study is shown in Fig. 1.

III. EXPERIMENTAL AND NUMERICAL SETUP

Experimental studies on interactions of focused wave and sheared currents with a vertical cylinder were performed in a wave–current flume at University College London (UCL). The experimental and numerical setup are presented in this section. The experimental measurements are used to validate the results of the numerical modeling with the vertical cylinder in place. In addition, the harmonic separation method applied to both experimental and numerical data is also presented in this section.

A. Experimental setup

The recirculating wave–current flume at UCL is 20 m long, 1.2 m wide, and 1 m depth with all experiments conducted in a water depth of 0.5 m. Two Edinburgh Design Limited force-feedback "piston-type" wavemakers are installed at each end of the flume. One wavemaker is used to generate waves, and the other is used to absorb waves actively. The flow entered the working section of the flume at approximately 1 m in front of the wavemaker.

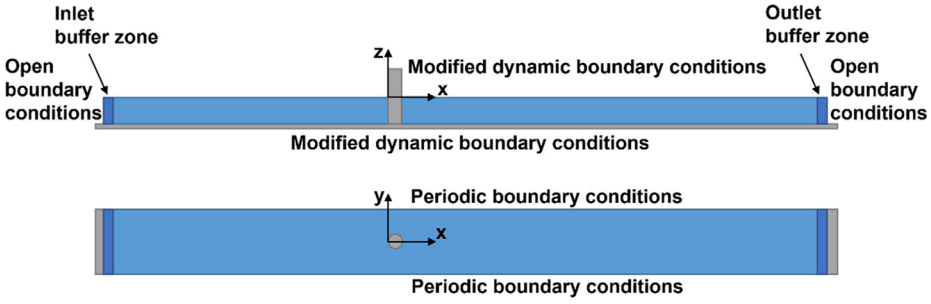

FIG. 1. General sketch of boundary conditions used in the numerical modeling. From top to bottom: side view and top view.

Focused waves were generated using a Gaussian target spectrum with a peak frequency f_p of 0.6 Hz and linear focused amplitude A_L of 0.07 m. The same target spectrum was used for generating focused waves on three different flow conditions (following sheared current, no current, and opposing sheared current). Surface elevation of a target wave group at $x = 0$ is defined as

$$\eta(t) = A\int_0^\infty S(\omega)\cos(\omega t + \Phi(\omega))\mathrm{d}\omega, \tag{12}$$

where A is a linear focus amplitude, and for a crest focused wave we set $\Phi(\omega) = 0$. A normalized Gaussian amplitude spectrum is

$$S(\omega) = \frac{1}{\omega_p\sigma\sqrt{2\pi}}\exp\left(-\frac{1}{2\sigma^2}\left(\frac{\omega}{\omega_p}-1\right)^2\right), \tag{13}$$

where $\omega_p = 2\pi f_p$ is a peak angular frequency. The bandwidth of the spectrum is controlled by a parameter σ, and we use $\sigma = 0.2898$. This provides a spectrum that occupies a range of frequencies from $\omega = 0$ to $\omega = 2\omega_p$, and we neglect parts of the spectrum beyond this range. The focusing point (FP) defined at $x = 0$ m was 8.7 m from the wavemaker. The amplitude matching point (AMP) is at $x = -4.7$ m. The return period was set to 128 s resulting in 256 wave components with frequency interval $\Delta f = 1/128$ Hz input to the wavemaker. The focal time was set to 64 s from the start of the wavemaker (focal time $t_f = 0$ s in this paper). For the detailed descriptions of the experimental setup, the reader can refer to Ref. 16. A general sketch of the wave–current flume is adapted from Ref. 16 and shown in Fig. 2. The surface elevation measured at the wave probe locations at $x = -4.7$ m and $x = -0.02$ m (0.02 m from the cylinder face) in the physical flume is used for the comparison with the SPH model.

B. Numerical setup

The time histories of horizontal velocities and surface elevation used as the inputs at the inlet of the SPH numerical wave–current flume are pre-computed by the Buldakov *et al.* model with the application of the iterative wave focusing methodology to reconstruct experimental surface elevation and kinematics of incoming focused waves and incoming focused waves on sheared currents. A truncated numerical flume compared with the physical flume is allowed owing to a full development of the combined wave–current conditions within this distance before interacting with the cylinder. A general sketch of the SPH numerical model is shown in Fig. 3. The domain length is 10 m, the damping zone length is 3 m, the water depth is 0.5 m, and the domain width is 1.2 m. For wave–current–structure interaction tests, the front face of the vertical cylinder (diameter $D = 0.25$ m) is located at the FP ($x = 0$ m), which is 8.7 m from the wavemaker in the physical flume and is 5 m from the inlet in the SPH numerical flume. The time of linear focus is defined as $t_f = 0$ s. The force provided by the post-processing software ComputeForces[38] provides values for the total instantaneous force including the combined effects of waves and currents.

Open boundaries are applied for the generation of wave-alone and wave–current conditions and for particles to leave or enter the fluid domain. At the inlet, time histories of horizontal velocities and surface elevation from the Buldakov *et al.* model are imposed, and density is extrapolated from the fluid domain. At the outlet, horizontal velocities are imposed according to the current profile, surface elevation is imposed according to the water depth, and density is extrapolated from the fluid domain. Only horizontal velocities are imposed at the inlet since no accuracy improvement can be gained by imposing vertical velocities and a negative impact on the particle spacing can occur.[40,62] It is suggested that at least eight layers of buffer particles

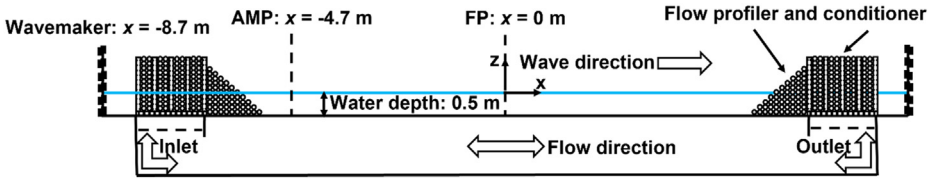

FIG. 2. General sketch of the wave–current flume at UCL, modified from Ref. 16.

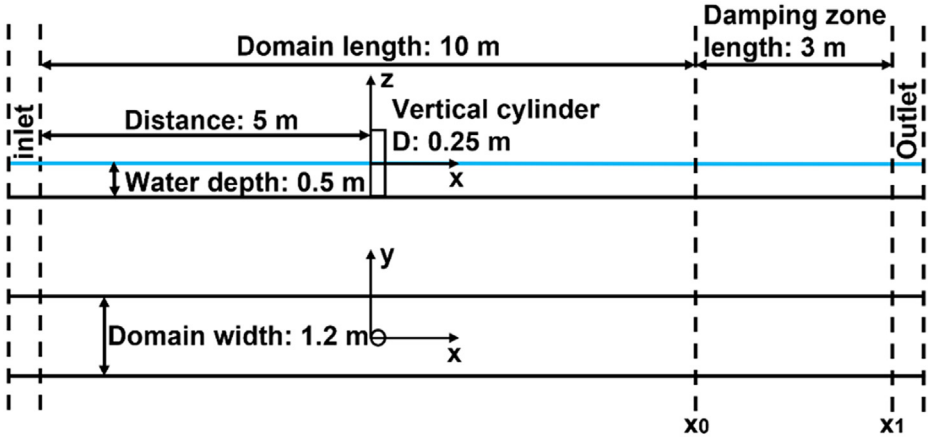

FIG. 3. General sketch of the SPH numerical model. From top to bottom: side view and top view.

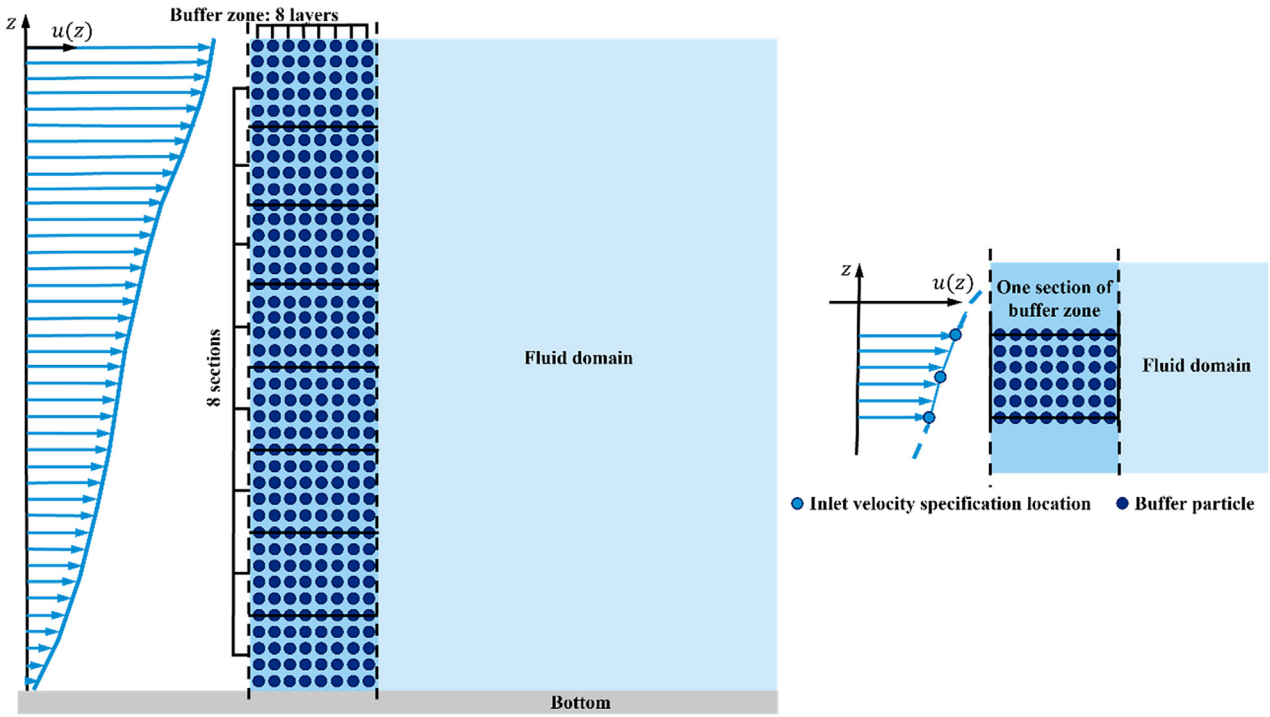

FIG. 4. General sketch of buffer zone at the inlet from Ref. 32. From left to right: the horizontal velocities imposing at the inlet and one section of the buffer zone at the inlet.

arranged in buffer zones can give accurate wave propagation simulations,[40] and this value is used in the present study.

Following the methodology presented in Ref. 32, the buffer zone at the inlet is divided into eight vertical sections in the present study. In each vertical section, the horizontal velocities (time series) are imposed at three different heights. The horizontal velocities at other heights in this section are obtained according to a parabolic fit function of DualSPHysics for each instant. A general sketch of the buffer zone at the inlet with the horizontal velocities imposing at the inlet and one section of the buffer zone is shown in Fig. 4.

A modified damping zone acting on the vertical velocity component is used for wave absorption when a current exists. A similar approach was applied in Ref. 63. In DualSPHysics, the velocity is reduced in the damping zone according to

$$\mathbf{v} = \mathbf{v}_0 \cdot f(x, \Delta t), \tag{14}$$

$$f(x, \Delta t) = 1 - \Delta t \cdot \beta \cdot \left(\frac{x - x_0}{x_1 - x_0}\right)^2, \tag{15}$$

where $\mathbf{v}_0$ is the initial velocity of the particle, $\mathbf{v}$ is the final velocity of the particle, $f(x, \Delta t)$ is the reduction function, Δt is the duration of the last time step, x is the position of particles, x_0 and x_1 are the initial and the final position of the damping zone, respectively, and β is the coefficient to modify the reduction function. When a current exists, only the vertical velocity component is reduced to absorb waves with $\beta = 100$ for the cases of focused waves on a following sheared current and focused waves on an opposing sheared current. Both the horizontal velocity component and vertical velocity component are reduced to absorb waves for the cases of focused waves only with $\beta = 10$.

C. Harmonic separation

Two focused wave groups generating with the phase shifts of 0° (crest focused waves) and 180° (trough focused waves) can be used to separate even and odd components.[64,65] With additional two focused wave groups generating with the phase shifts of 90° and 270°, these time histories of surface elevation (S) and force (F) can be used to achieve a more effective separation. Figure 5 shows an example of surface elevations at the focal location of focused wave groups generated with the phase shifts of 0°, 90°, 180°, and 270°.

Four focused wave groups are generated with the phase shifts of 0° (obtain time histories S_0 and F_0), 90° (S_{90} and F_{90}), 180°

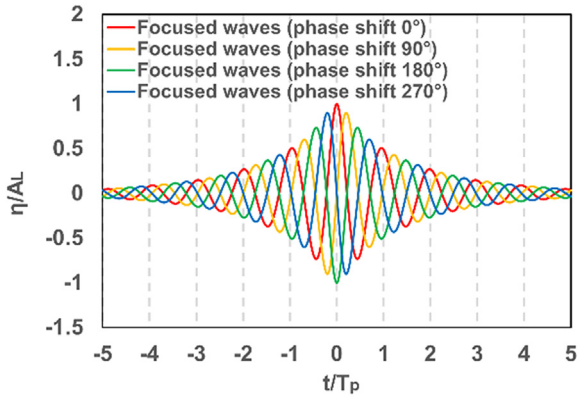

FIG. 5. An example of surface elevations at the focal location of focused wave groups generating with different phase shifts.

(S_{180} and F_{180}), and 270° (S_{270} and F_{270}). Then, the Hilbert transform is applied to the surface elevation time histories S_{90} and S_{270} to obtain S_{90}^H and S_{270}^H and applied to the force time histories F_{90} and F_{270} to obtain F_{90}^H and F_{270}^H. Taking force as an example (using the same approach for the extraction of harmonics for surface elevation), harmonic components can be extracted by the following linear combinations of these time histories and their Hilbert transforms:[14,17,18,20,21]

$$\frac{(F_0 + F_{90} + F_{180} + F_{270})}{4} = A^2 f_{2,0} + A^4 f_{4,0} + A^4 f_{4,4}\cos 4\varphi + O(A^6), \tag{16}$$

$$\frac{(F_0 - F_{90}^H - F_{180} + F_{270}^H)}{4} = A f_{1,1}\cos\varphi + A^3 f_{3,1}\cos\varphi + O(A^5), \tag{17}$$

$$\frac{(F_0 - F_{90} + F_{180} - F_{270})}{4} = A^2 f_{2,2}\cos 2\varphi + A^4 f_{4,2}\cos 2\varphi + O(A^6), \tag{18}$$

$$\frac{(F_0 + F_{90}^H - F_{180} - F_{270}^H)}{4} = A^3 f_{3,3}\cos 3\varphi + O(A^5), \tag{19}$$

where f refers to the extracted force components, the first combination extracts the second-order subharmonic and fourth-order superharmonic (these two can be separated by frequency filtering), and the last three combinations extract the first-order (linear) harmonic, second-order superharmonic, and third-order superharmonic, respectively, with negligible higher-order terms. A fast Fourier transform (FFT) can be applied to the time history signals of different harmonic components to obtain the amplitude spectra.

IV. MODEL VALIDATION AND HARMONIC ANALYSIS

The implementation of the SPH-based numerical wave–current flume and modeling of wave–current–structure interactions in the model is validated in this section. The wave–current generation method is first validated with the Buldakov *et al.* model for surface elevation and velocity profile in Sec. IV A to demonstrate the accuracy of generation of wave–current conditions. The numerical modeling of interactions of focused waves and sheared currents with the cylinder is validated with experiments for surface elevation and horizontal force on the cylinder in Sec. IV B to demonstrate the model's capability for modeling wave–current–structure interaction. The harmonic analysis is performed using the method described in Sec. III C, and the results are validated with experiments in Sec. IV C. The convergence study with computational performance is presented in Sec. IV D.

A. Wave–current conditions

The sheared current profiles imposed in the SPH numerical model and their comparison with the profiles used in the Buldakov *et al.* model (referred to as LaNM in the figure legends) are shown in Fig. 6. The current profiles in the Buldakov *et al.* model were approximated according to the current profiles measured in the experiments. The sheared current profile is also imposed at the outlet of the SPH numerical model.

The surface elevations are measured at the AMP ($x = -4.7$ m) and the FP ($x = 0$ m). At the FP, the horizontal velocity profile is measured at the focal time. The measured numerical results for three cases of focused waves on a following sheared current, focused waves only, and focused waves on an opposing sheared current are compared with the Buldakov *et al.* model in Fig. 7, demonstrating the accuracy of conditions generated in the SPH numerical model. Previous particle refinement studies showing convergence for focused waves and currents can be found in Ref. 32. Figure 8 shows the simulation snapshot of the horizontal velocity field at the focal time for focused waves on a following sheared current, focused waves only, and focused waves on an opposing sheared current.

B. Cylinder loading

The measured surface elevations from the SPH numerical model are compared with the surface elevations measured at two of the wave probe locations (the AMP: $x = -4.7$ m, and at the front face of the cylinder close to the FP: $x = -0.02$ m) in the experiments. The measured horizontal forces on the cylinder from the SPH numerical model are also compared with the measured ones in the experiments in this section. As suggested in Ref. 37 for the simulation of focused waves impacting a cylinder using ISPH, the particles of the cylinder are arranged in terms of radial arrangement instead of a Cartesian arrangement, and both arrangements are shown in Fig. 9.

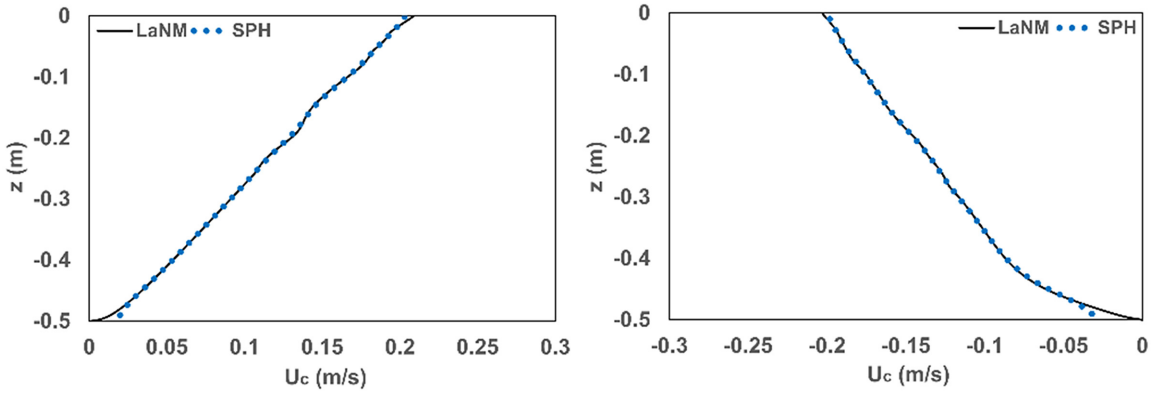

FIG. 6. Comparison between the sheared current profiles in the SPH numerical model (imposed) and in the Buldakov *et al.* LaNM model. From left to right: a following sheared current and an opposing sheared current.

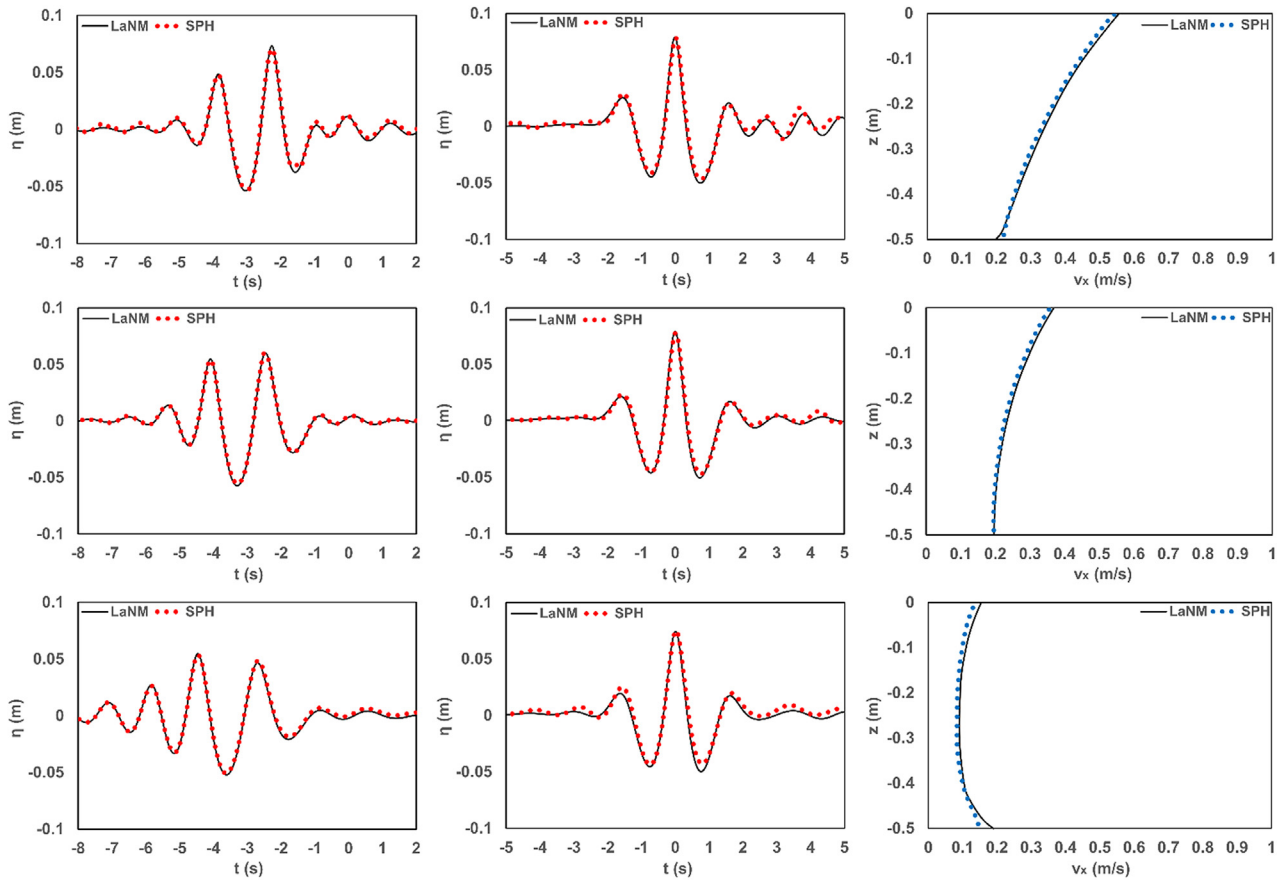

FIG. 7. Comparison between the numerical results in the SPH numerical model and in the Buldakov *et al.* LaNM model for crest focused waves. From top to bottom: following sheared current case, no current case, and opposing sheared current case. From left to right: surface elevation at $x = -4.7$ m, surface elevation at $x = 0$ m, and horizontal velocity profile at the focal location (FP) and focal time.

The measured numerical results for focused waves on a following sheared current, focused waves only, and focused waves on an opposing sheared current are compared with the experiments (referred to as EXP) in Fig. 10, demonstrating the accuracy of modeling wave–current–structure interactions in the SPH numerical model. Figure 11 shows the simulation snapshot of the horizontal velocity field at the focal time with the cylinder in place for focused waves on a following sheared current, focused waves only, and focused waves on an opposing sheared current. Four focused wave groups are generated with phase shifts of 0°, 90°, 180°, and 270°. For focused wave groups generated with phase shifts of 90°, 180°, and 270°, the measured numerical results of the surface elevations at the AMP and at the front face of the cylinder close to the FP and the horizontal forces on the cylinder are compared with the experiments and given in the Appendix. The velocity fields are shown to be smooth and in good agreement with the experiments. Some very small noise is noted to exist in the velocity and associated pressure fields. In the present study, the coefficient in the viscosity term in the momentum equation is set to 0.001 to limit the effects of artificial viscosity on wave propagation. In addition to artificial viscosity, there are new treatments emerging, which offer the possibility to reduce this unphysical noise including the velocity-divergence error mitigating (VEM) and volume conservation shifting (VCS) schemes in Ref. 66 or an acoustic damper term in Ref. 67. Alternatively, the pressure values can be filtered during post-processing.[68]

C. Harmonic analysis

Using the harmonic separation method described in Sec. III C, the second-order subharmonic, the linear signal and the first three superharmonics (to fourth-order) are obtained for the surface elevation at the front face of the cylinder and the horizontal force on the cylinder based on the numerical results in Sec. IV B and the Appendix. The second-order subharmonic and the fourth-order superharmonic are separated by frequency filtering. The frequency range is $0 < f/f_p < 1$ for the second-order subharmonic as also used in Ref. 16 and $3 < f/f_p < 5$ for the fourth-order superharmonic according to $Nf_p - f_p < f < Nf_p + f_p$ $(N = 4)$. The harmonic components of the free-surface elevation at the front face of the cylinder and the horizontal force on the cylinder are shown in Figs. 12 and 13, respectively. Time histories of the separated harmonics (second-order subharmonic, linear harmonic, second-order superharmonic, third-order superharmonic, and fourth-order superharmonic) for focused waves on three different flow conditions (following sheared current case, no current case, and

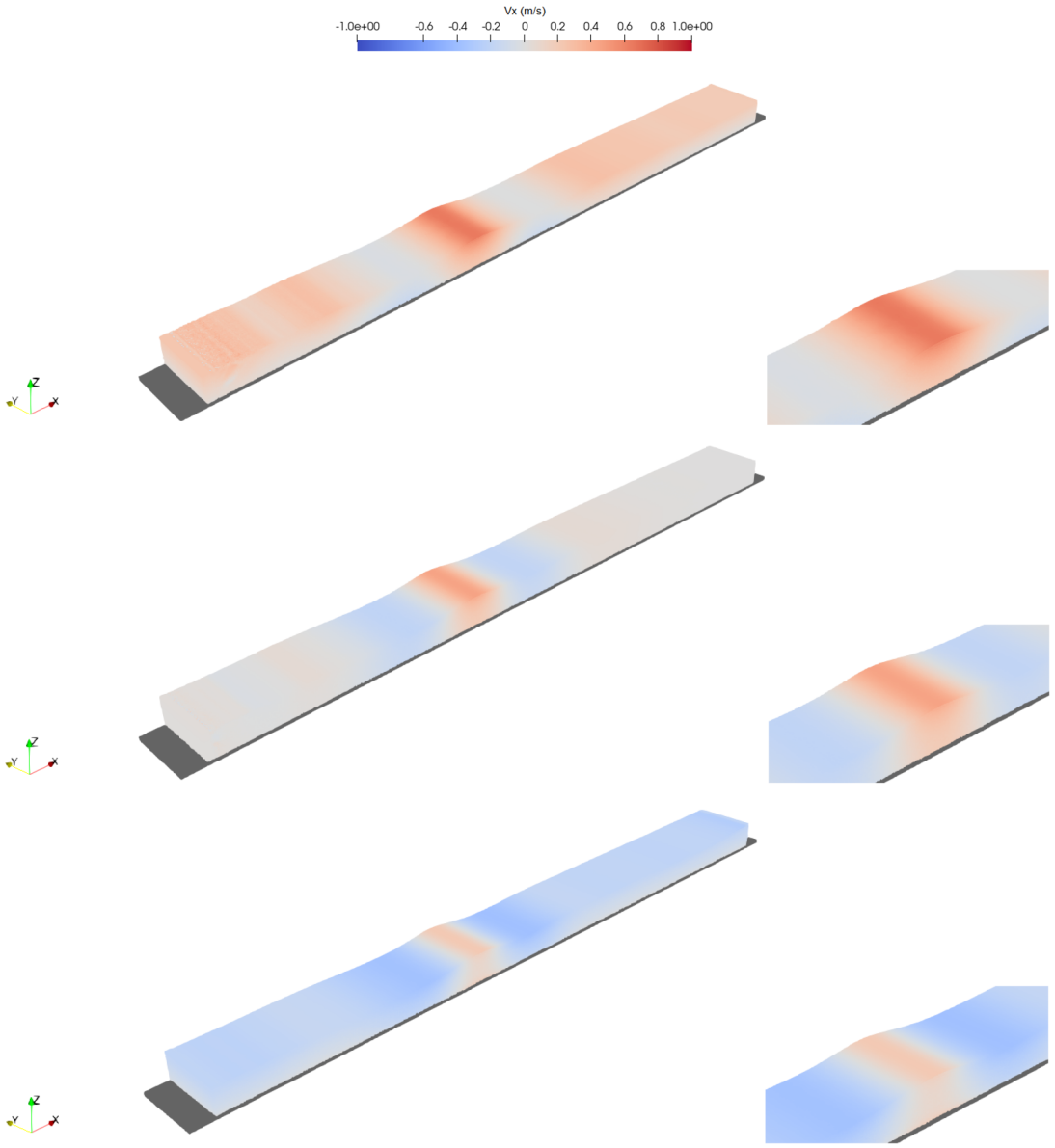

FIG. 8. Simulation snapshot of the horizontal velocity field at the focal time for crest focused waves. From top to bottom: following sheared current case, no current case, and opposing sheared current case.

opposing sheared current case) are given. An overall good agreement between harmonic components obtained from experimental measurements and numerical results is achieved. However, less good agreement is found for second-order subharmonic and third-order superharmonic as in Ref. 16. The second-order subharmonic discrepancy is likely to do with the difference in the generated subharmonic error waves between the experiments and combined numerical modeling approach.

D. Convergence study

The initial interparticle distance d_p (0.0125 m) used in the simulations in Sec. IV A, Sec. IV B, and the Appendix has been shown to provide accurate results. However, a convergence study for crest focused waves on a following sheared current, crest focused waves only, and crest focused waves on an opposing sheared current with the cylinder in place has been performed, respectively. The measured horizontal forces on the cylinder from the SPH numerical model are compared with the measured ones in the experiments with four different values of d_p (0.03125, 0.025, 0.02, and 0.0125 m) in Fig. 14. Values of d_p in the convergence study were selected so that the ratio d/d_p is an integer, which is recommended in Ref. 39. As d_p reduces, the agreement with experiments improves. In order to quantify the accuracy of the simulations with different values of d_p, the Root Mean Square

FIG. 9. Arrangements of the particle distribution for the cylinder. From left to right: Cartesian arrangement and radial arrangement.

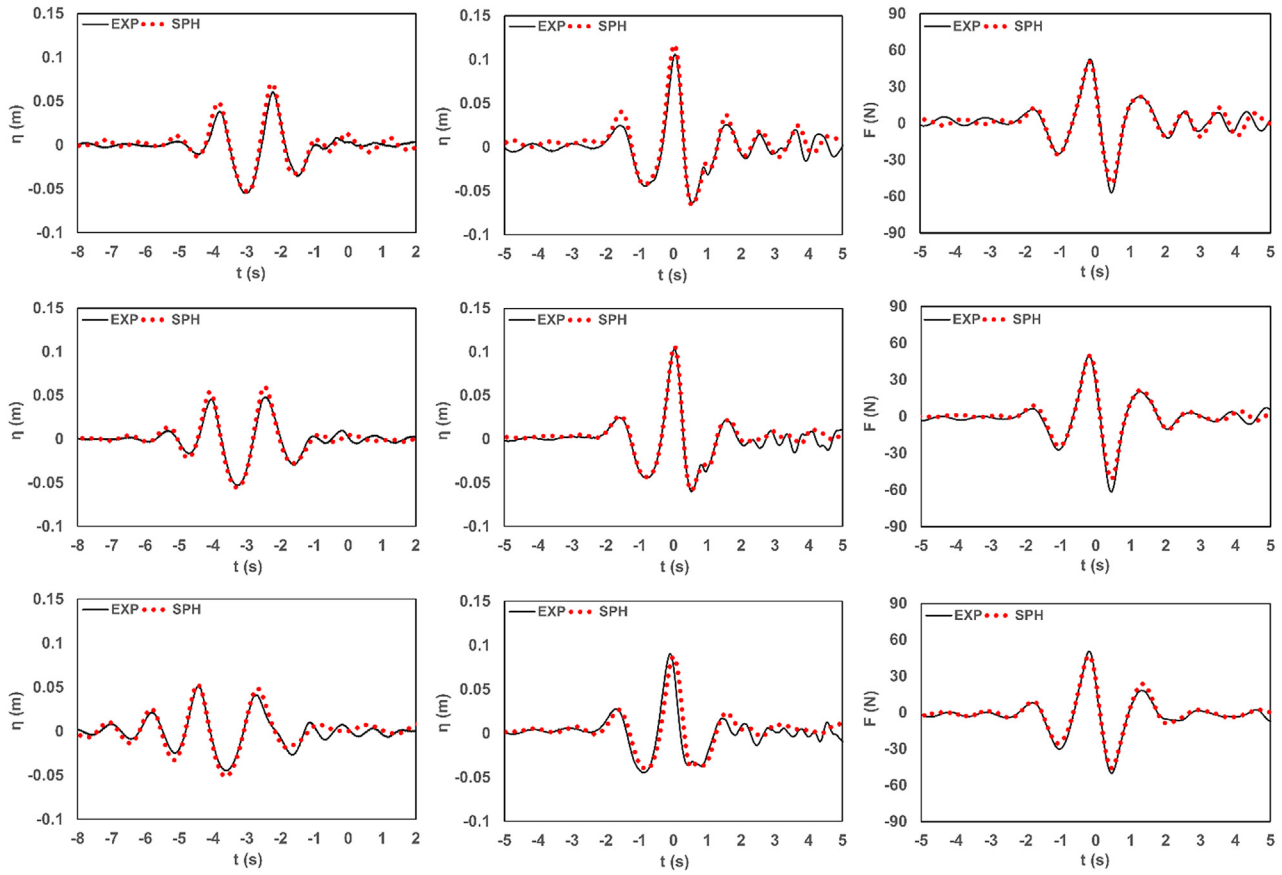

FIG. 10. Comparison between the numerical results in the SPH numerical model and measurements in the experiments for crest focused waves. From top to bottom: following sheared current case, no current case, and opposing sheared current case. From left to right: surface elevation at $x = -4.7$ m, surface elevation at $x = -0.02$ m, and horizontal force on the cylinder.

Error (RMSE) value over time for the horizontal force on the cylinder [e.g., from $t = t_1$ $(i = 1)$ to $t = t_n$ $(i = n)$] is calculated as follows:

$$RMSE(F) = \frac{1}{\max_i \left(F(t_i)^{\mathrm{EXP}}\right)} \sqrt{\frac{1}{n}\sum_{i=1}^{n}\left(F(t_i)^{SPH} - F(t_i)^{\mathrm{EXP}}\right)^2}. \tag{20}$$

The RMSE values (time histories of horizontal force based on a 10 s time duration from −5 to 5 s), runtime (for 15 s of physical time), and total number of particles (N_p) are listed in Table I. Using a finer resolution (0.0125 m) improves the accuracy of the simulation compared with the other resolutions (0.02, 0.025, and 0.03125 m) with the RMSE value decreasing for all the following sheared current case, the no current case, and the opposing sheared current case.

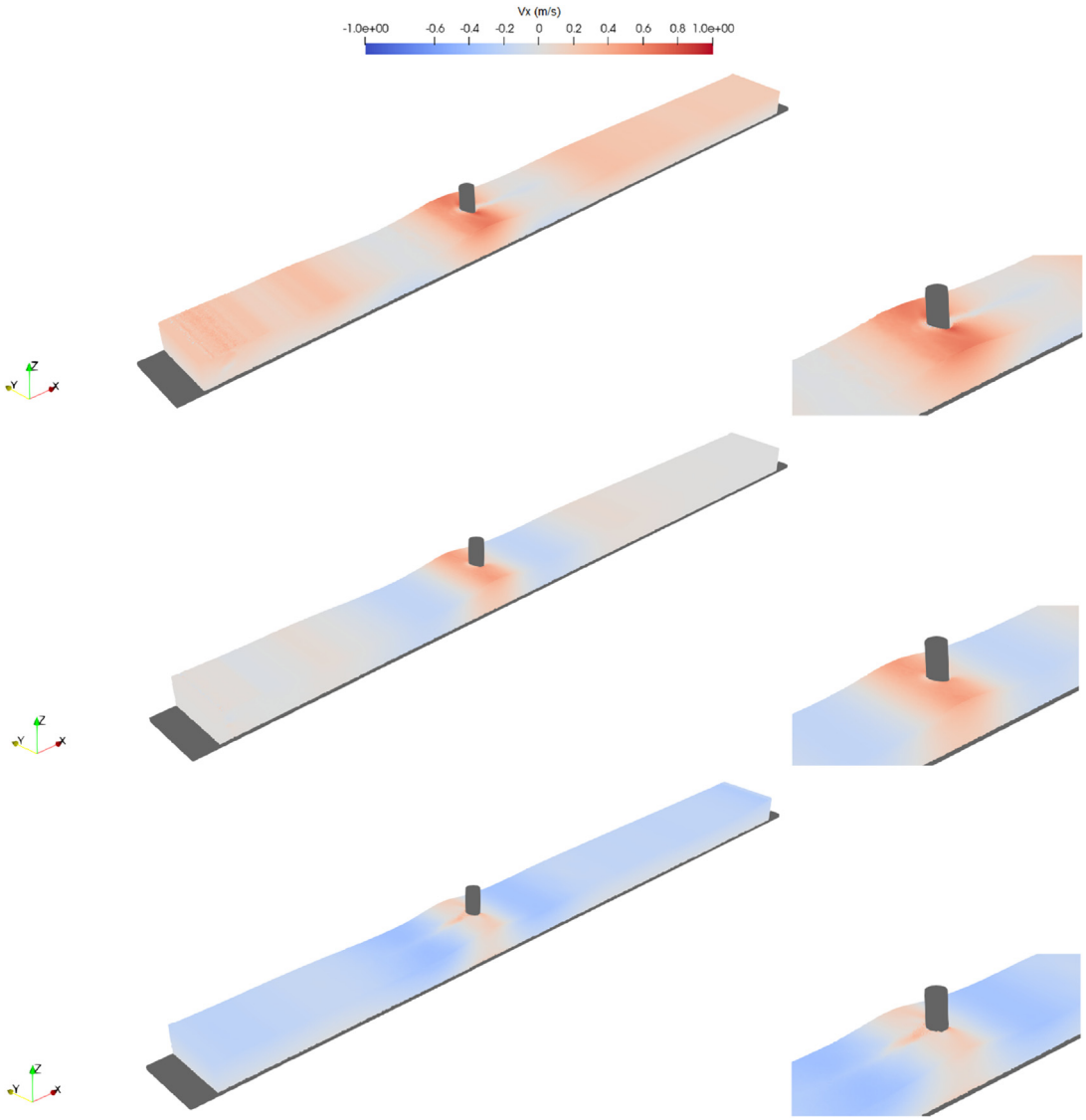

FIG. 11. Simulation snapshot of the horizontal velocity field at the focal time with the cylinder in place for crest focused waves. From top to bottom: following sheared current case, no current case, and opposing sheared current case.

The computational performance of DualSPHysics on GPUs for modeling wave–structure interactions and wave–current–structure interactions is of practical importance for research and engineering. The computational times in the present study are on the order of hours. All simulations in this section were computed on an Nvidia GeForce RTX 3080 Laptop GPU.

V. PEAK FORCE IN STEEP AND BREAKING WAVES ON SHEARED CURRENTS

The model validation in Sec. IV and the Appendix demonstrates a high accuracy for modeling wave–current–structure interaction in the SPH numerical model in the present study. In this section, the sensitivity of peak force on the cylinder in steep and breaking focused waves with phase shifts of 0°, 90°, 180°, and 270° on different flow conditions is investigated. Wave amplitudes are increased up to, and beyond, the breaking threshold. The methodology for increasing wave amplitude is presented in Sec. V A. The sensitivity of peak force with increasing wave amplitude for different focused wave phases is presented in Sec. V B. The comparison with the Morison equation is given in Sec. V C.

A. Methodology for increasing wave steepness

The time histories of surface elevation used as the inputs at the inlet of the SPH numerical wave–current flume (pre-computed by the Buldakov *et al.* model) are used to extract the first-order (linear) harmonic according to Eq. (17). A Fourier transform is applied to the time histories of the first-order (linear) harmonic to obtain the wave

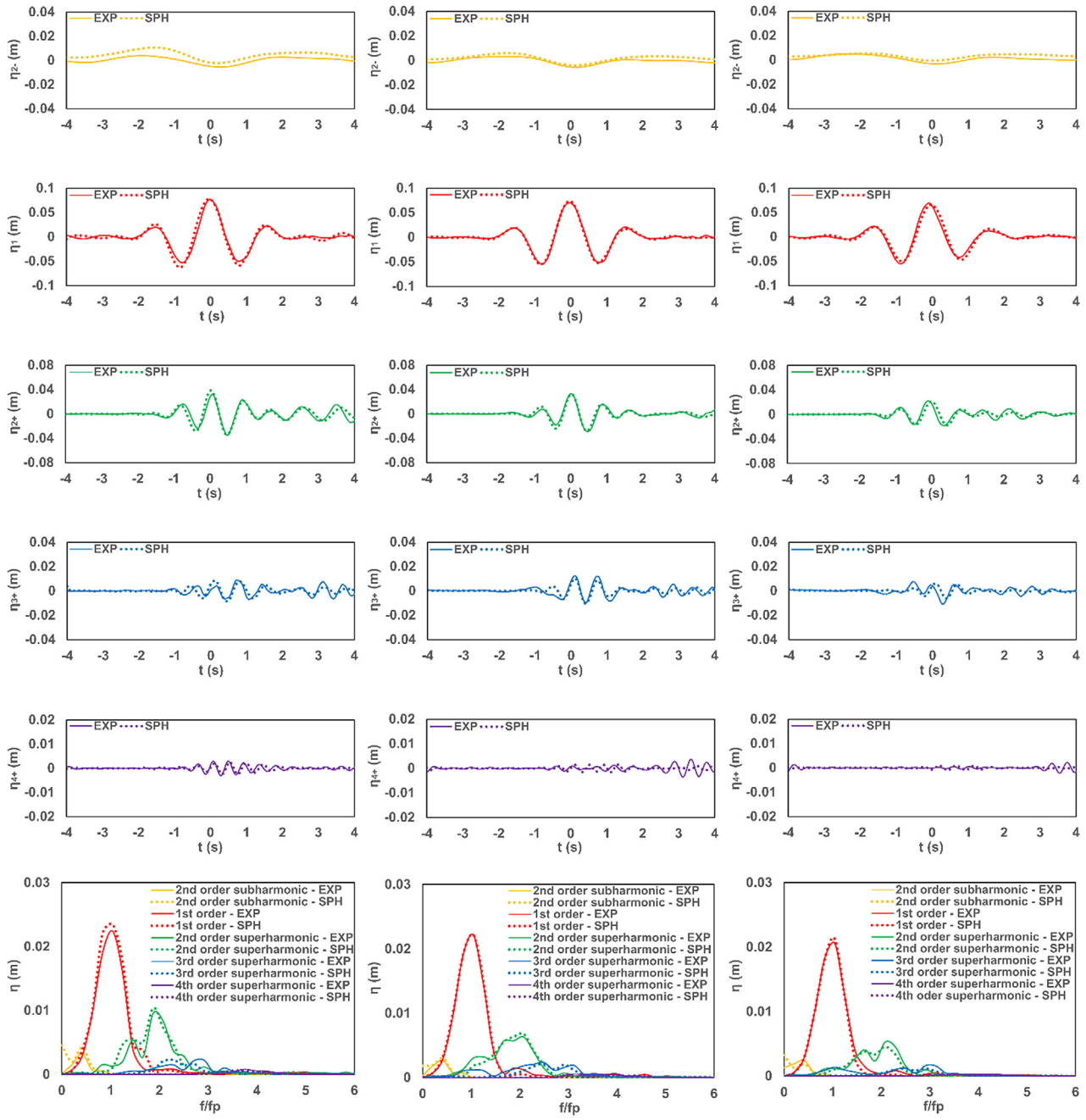

FIG. 12. Harmonic components of the free surface elevation at the front face of the cylinder. From left to right: following sheared current case, no current case, and opposing sheard current case. From top to bottom: second-order subharmonic, linear harmonic, second-order superharmonic, third-order superharmonic, fourth-order superharmonic, and amplitude spectra of the free surface elevation.

amplitude a_i of each wave component. The wavenumber of each wave component is obtained by the standard linear dispersion relation for focused waves only and the modified dispersion relation considering a linearly sheared current with constant vorticity across the water depth[69] for focused waves on a current. The standard linear dispersion relation and the modified dispersion relation are given as follows:

$$\omega^2 = gk\tanh(kd), \tag{21}$$

$$(\omega - kU_s)^2 = \left(gk - \Omega_s(\omega - kU_s)\right)\tanh(kd), \tag{22}$$

where g is the acceleration due to gravity, d is the water depth, ω is the angular frequency, k is the wavenumber, U_s is the surface current, and Ω_s is the constant vorticity equal to U_s/d. The global steepness is

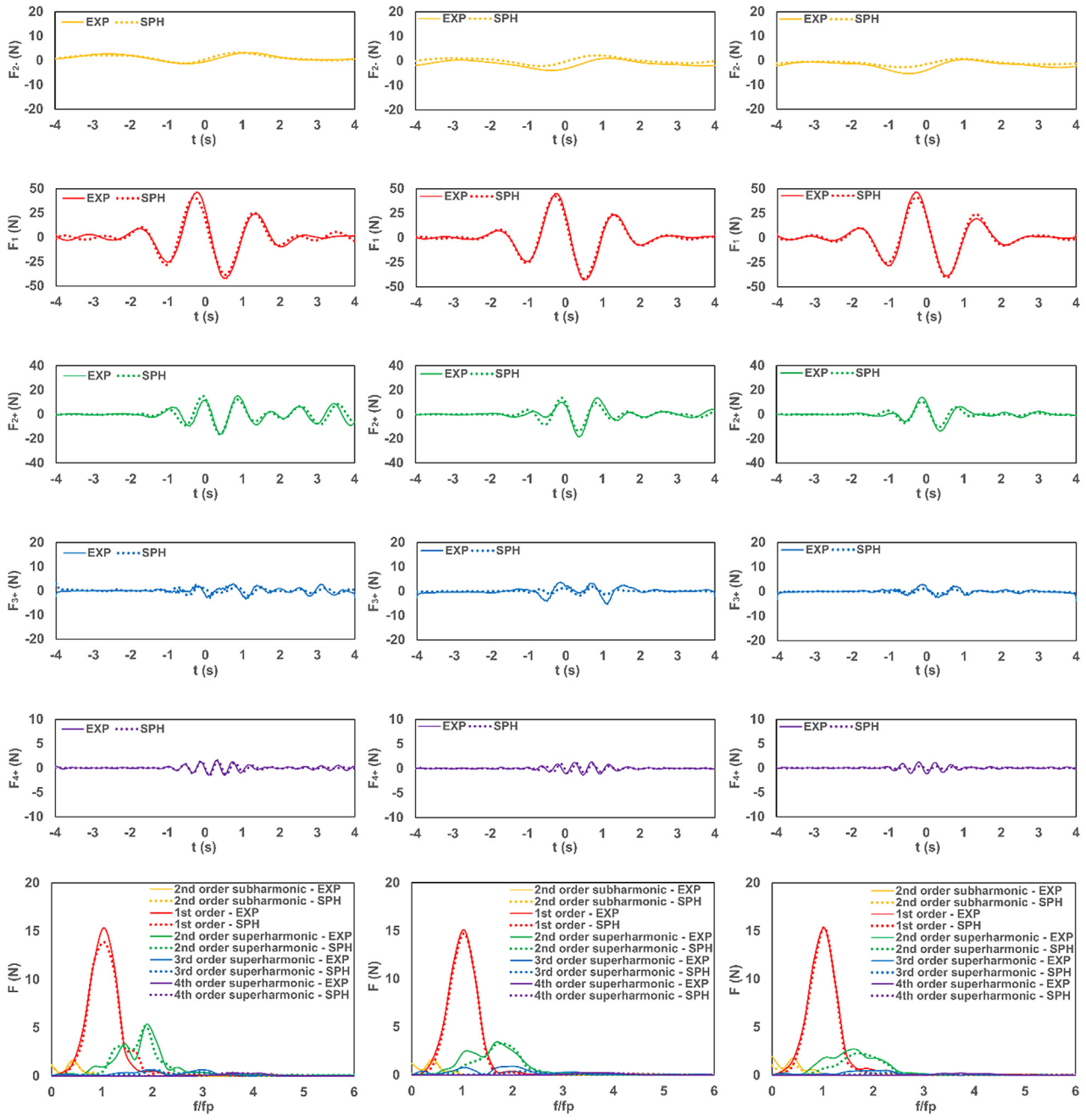

FIG. 13. Harmonic components of the horizontal force on the cylinder. From left to right: following sheared current case, no current case, and opposing sheared current case. From top to bottom: second-order subharmonic, linear harmonic, second-order superharmonic, third-order superharmonic, fourth-order superharmonic, and amplitude spectra of the horizontal force.

obtained by $\sum k_i a_i$ (defined as original $\sum k_i a_i$), and they are 0.143, 0.153, and 0.172 for focused waves on a following sheared current, focused waves only, and focused waves on an opposing sheared current, respectively. The initial target $\sum k_i a_i$ is set to 0.2 and then increased in 0.05 increments until the breaking is found. The time histories of wave-induced horizontal velocities and surface elevation at the inlet are modified by multiplying the ratio between target $\sum k_i a_i$ and original $\sum k_i a_i$. For generation of focused waves on a current, the time histories of horizontal velocities at the inlet are obtained by the superposition of modified wave-induced horizontal velocities and

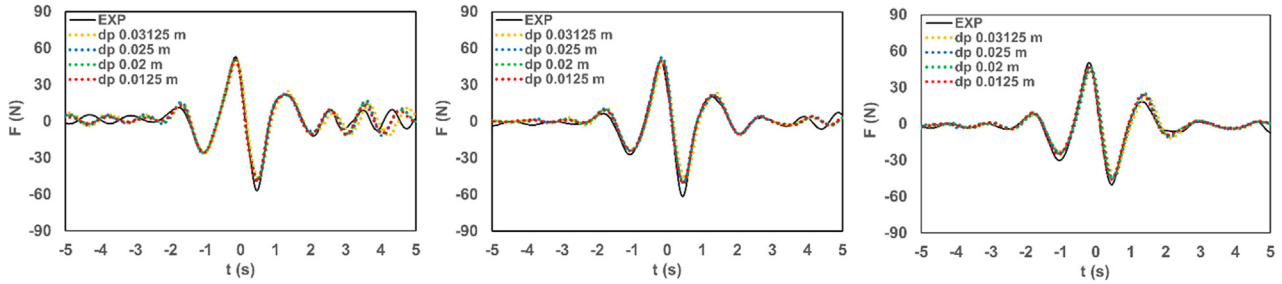

FIG. 14. Horizontal force on the cylinder for different initial interparticle distances for crest focused waves. From left to right: following sheared current case, no current case, and opposing sheared current case.

TABLE I. RMSE values, runtimes, and number of particles N_p with different resolutions d_p for the case of crest focused waves.

	Following sheared current		No current		Opposing sheared current	
d_p (m) (N_p [10^6])	*RMSE*(F)	*Runtime* (h)	*RMSE*(F)	*Runtime* (h)	*RMSE*(F)	*Runtime* (h)
0.03125 (0.33)	0.126	0.262	0.108	0.241	0.089	0.252
0.025 (0.62)	0.096	0.523	0.074	0.538	0.068	0.529
0.02 (1.17)	0.083	1.172	0.071	1.190	0.052	1.172
0.0125 (4.50)	0.076	6.335	0.061	6.230	0.044	6.266

the current profile. Then, the modified time histories of horizontal velocities and surface elevation are used as the inputs at the inlet of the SPH numerical wave–current flume. It is to be noted that this approach is only approximate as we apply a linear scaling approach to nonlinear signals of elevation and velocity. Due to the broadbanded nature of the wave groups, however, dispersive effects mean that the waves are relatively linear at the inlet position with the linear contribution accounting for around 90% of the total elevation. We, therefore, use this approximate approach to further demonstrate the model's ability at modeling steep and breaking wave loads in the presence of sheared currents and how wave amplitude and breaking affects peak loads. We do not, however, assess the separated harmonics due to the approximate generation of the bound harmonics using this approach.

B. Sensitivity of peak force with increasing wave amplitude

As shown in Sec. IV D, though a finer resolution gives a closer agreement with experimental data, d_p (0.02 m) gives a very similar results compared with d_p (0.0125 m) with a considerably shorter runtime. Thus, all the results presented in Sec. V B are using d_p (0.02 m). We find significantly different breaking threshold steepness values for the three current profiles. The breaking thresholds are identified visually from the SPH simulations and are found between $\sum k_i a_i = 0.2$ and $\sum k_i a_i = 0.25$ for crest focused waves on a following sheared current, between $\sum k_i a_i = 0.3$ and $\sum k_i a_i = 0.35$ for crest focused waves only, and between $\sum k_i a_i = 0.4$ and $\sum k_i a_i = 0.45$ for crest focused waves on an opposing sheared current.

We believe these differences in breaking threshold steepness can be explained partially by the modified ratios of total surface particle velocity (=wave-induced particle velocity + current surface velocity at the surface) relative to the current-modified phase speed. The increase in the breaking threshold steepness in negative shear can be explained by the reduction of the total surface particle velocity (=a negative surface current + current-modified wave-induced particle velocity) relative to the phase speed. Similarly, the positive shear increases the total surface particle velocity relative to the phase speed, and thus, breaking onset occurs at a lower steepness. This is consistent with the conclusion in Ref. 45 that a reduction in wave steepness at the breaking threshold is found proportional to the magnitude of the velocity gradient. However, the contribution of the approximate scaling methodology, and associated errors in the bound wave structure, could also affect these preliminary results. These findings do warrant a significant future study on the effect of shear profile on breaking steepness, which is out of the scope of this paper.

The maximum target values of $\sum k_i a_i$ are 0.3, 0.35, and 0.45 for focused waves on a following sheared current, focused waves only, and focused waves on an opposing sheared current, respectively, to obtain breaking waves for all focused wave groups with phase shifts of 0°, 90°, 180°, and 270°. The maximum value of the surface elevation at the front face of the cylinder ($x = -0.05$ m) and the positive peak horizontal force on the cylinder are plotted as a function of $\sum a_i$ in Figs. 15 and 16. According to Fig. 16, among four focused wave groups generated with the phase shifts of 0°, 90°, 180°, and 270°, it was found that the maximum positive peak horizontal force on the cylinder is obtained in focused waves generated with phase shift 270° for two flow conditions (focused waves only and focused waves on an opposing sheared current). For focused waves on a following sheared current, focused waves generated with phase shift 0° give a slightly larger positive peak horizontal force on the cylinder than focused waves generated with phase shift 270° (200.8 N and 196.5 N). This is contrary to that expected from linear theory for an inertia dominated structure where peak forces would be expected for the 90° phase shift condition

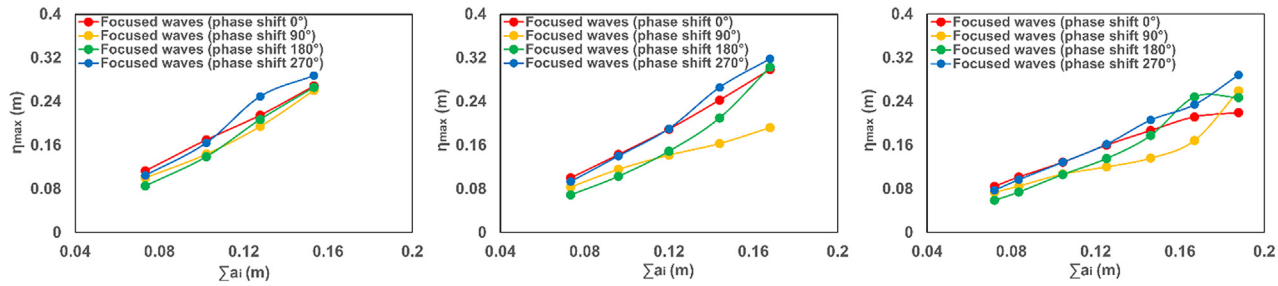

FIG. 15. The maximum value of the free surface elevation at the front face of the cylinder with increased wave amplitude. From left to right: focused waves on a following sheared current, focused waves only, and focused waves on an opposing sheared current.

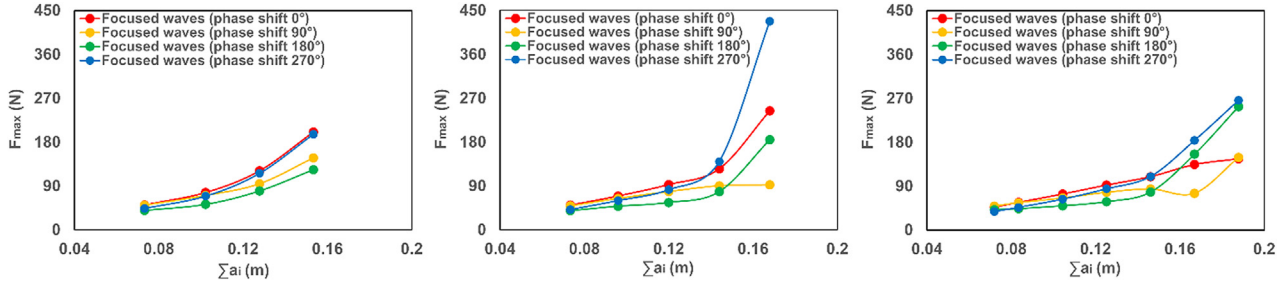

FIG. 16. The positive peak horizontal force on the cylinder with increased wave amplitude. From left to right: focused waves on a following sheared current, focused waves only, and focused waves on an opposing sheared current.

TABLE II. The normalized times $(t - t_f)/T_p$ when the cylinder experiences the positive peak horizontal force at original $\sum k_i a_i$ (and largest $\sum k_i a_i$).

	Following sheared current original (largest)	No current original (largest)	Opposing sheared current original (largest)
0° focused waves	−0.09 (−0.18)	−0.09 (−0.195)	−0.105 (−0.21)
90° focused waves	0.18 (0.195)	0.165 (0.18)	0.165 (−1.05)
180° focused waves	0.435 (−0.69)	0.39 (−0.78)	0.36 (−0.885)
270° focused waves	−0.375 (−0.495)	−0.36 (−0.555)	−0.36 (−0.57)

where components are focused in such a way to provide maximum acceleration. Although this appears to be the case for the more linear conditions (lower $\sum a_i$), this is no longer the case for larger waves. The results demonstrate extreme sensitivity of maximum force to the wave phase and hence equivalently the relative location of the cylinder to a large wave event, suggesting different phases/relative locations should routinely be considered in design.

To assess this relationship further, we look at the times where maximum forces are recorded, relative to the focal time, for each condition. The times when the cylinder experiences the positive peak horizontal force are presented in Table II. These are shown for the original and the largest $\sum k_i a_i$ values normalized according to $(t - t_f)/T_p$ (linear focal time t_f is 0 s). These values further highlight the complex relationship between the phase of the waves and the peak force as the times where peak force are expected, based on the linear theory, for an inertia dominated structure are not what we observe in the outputs. For example, the maximum value of acceleration and hence expected

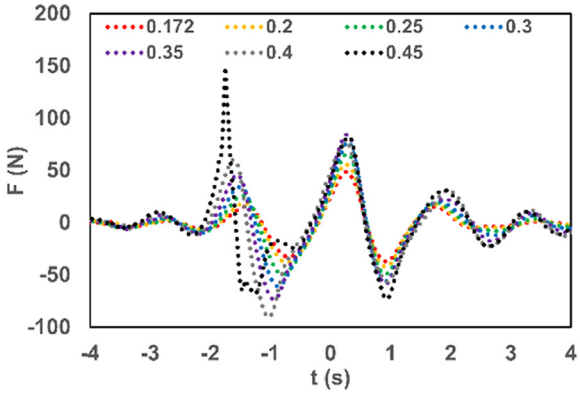

FIG. 17. Horizontal force on the cylinder for focused waves generating with phase shift 90° on an opposing sheared current with different values of $\sum k_i a_i$.

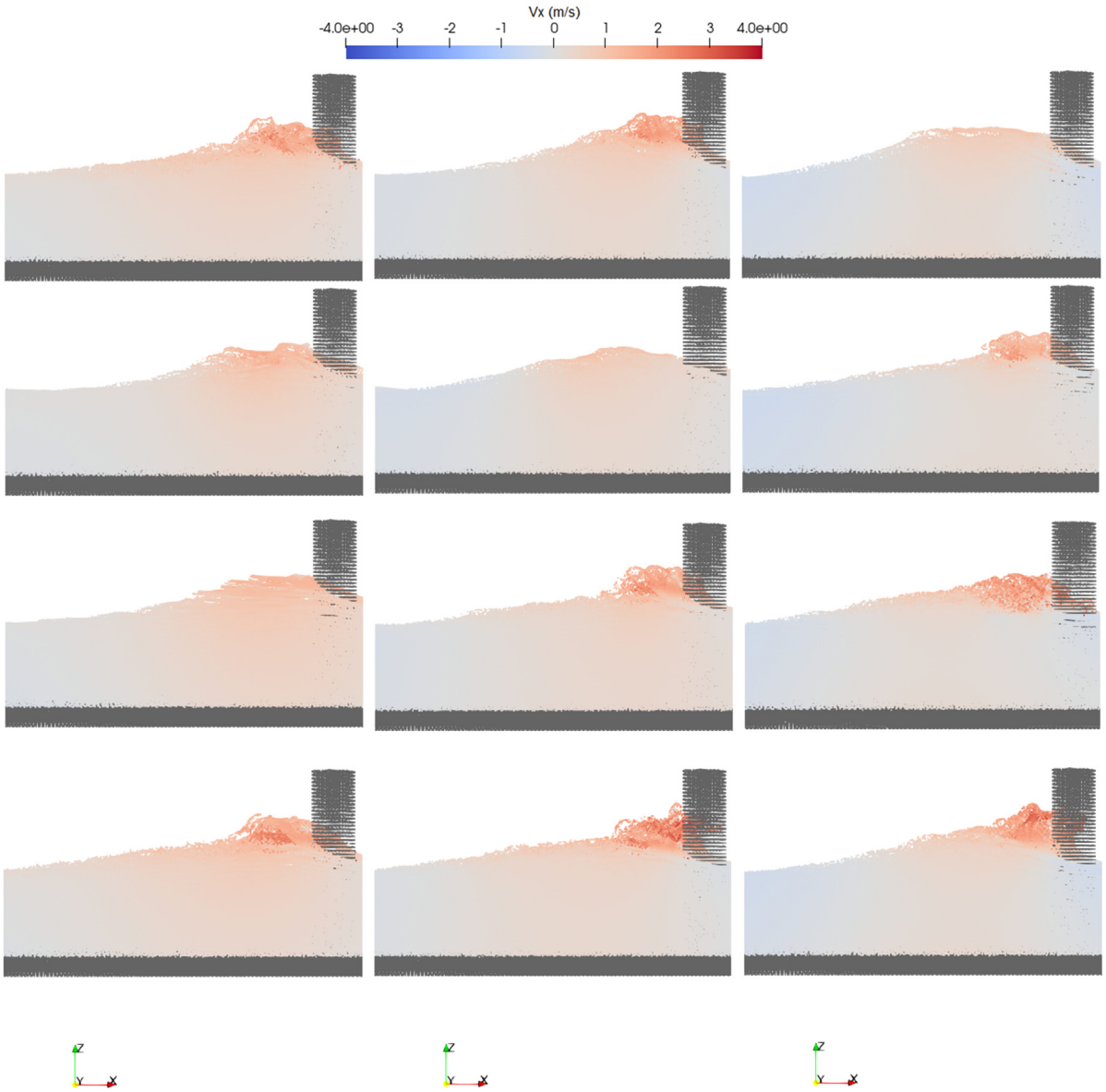

FIG. 18. Simulation snapshot of the horizontal velocity field at the instant when cylinder is subject to positive peak horizontal force. From top to bottom: focused waves generated with a phase shift 0°, 90°, 180°, and 270°, respectively. From left to right: following sheared current case, no current case, and opposing sheared current case.

TABLE III. The values of C_M for focused wave groups with the phase shifts of 0° at original $\sum k_i a_i$ (and different $\sum k_i a_i$) and for focused wave groups with the phase shifts of 90°, 180°, and 270° at original $\sum k_i a_i$.

	Following sheared current 0.143 (0.2, 0.25, 0.3)	No current 0.153 (0.2, 0.25, 0.3, 0.35)	Opposing sheared current 0.172 (0.2, 0.25, 0.3, 0.35, 0.4, 0.45)
0° focused waves	2.10 (2.03, 1.93, 2.06)	2.05 (2.03, 2.01, 1.97, 2.04)	2.00 (2.00, 2.00, 2.00, 1.96, 1.97, 1.95)
90° focused waves	2.12	2.06	2.01
180° focused waves	2.13	2.06	2.02
270° focused waves	2.12	2.05	1.99

TABLE IV. The values of C_D for focused wave groups with the phase shifts of 0° at original $\sum k_i a_i$ (and different $\sum k_i a_i$) and for focused wave groups with the phase shifts of 90°, 180°, and 270° at original $\sum k_i a_i$.

	Following sheared current 0.143 (0.2, 0.25, 0.3)	No current 0.153 (0.2, 0.25, 0.3, 0.35)	Opposing sheared current 0.172 (0.2, 0.25, 0.3, 0.35, 0.4, 0.45)
0° focused waves	1.28 (1.46, 1.42, 0.95)	2.27 (2.08, 1.97, 1.65, 1.14)	0.49 (0.56, 0.75, 0.89, 1.03, 1.16, 1.43)
90° focused waves	1.22	2.02	0.41
180° focused waves	1.18	1.42	0.46
270° focused waves	1.24	1.96	0.43

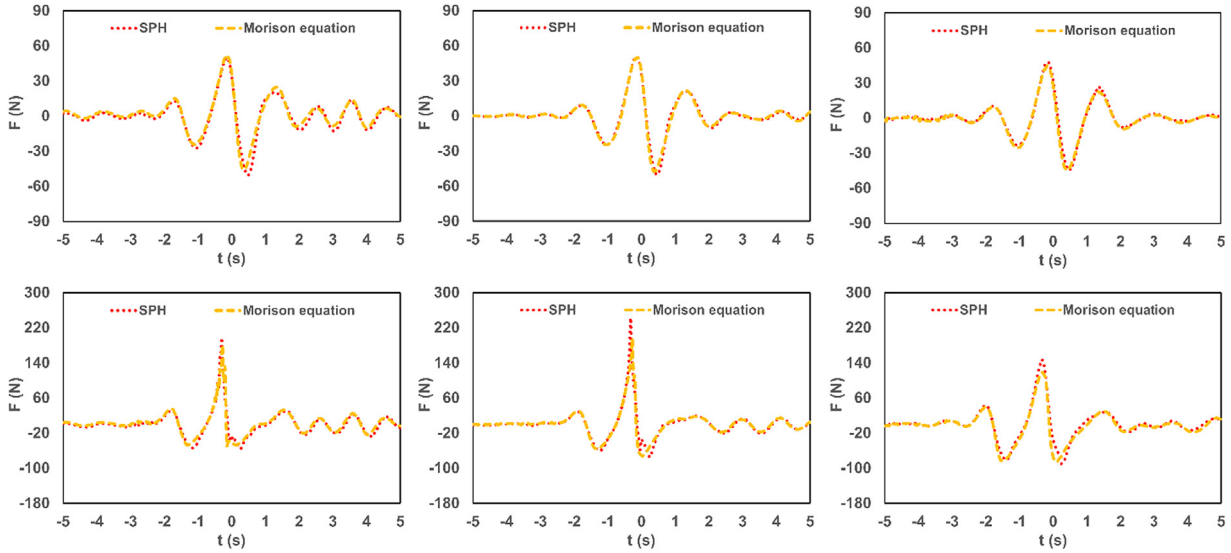

FIG. 19. Comparison between the results in the SPH numerical model and results using the Morison equation for crest focused waves. From top to bottom: original $\sum k_i a_i$ and largest $\sum k_i a_i$. From left to right: following sheared current case, no current case, and opposing sheared current case.

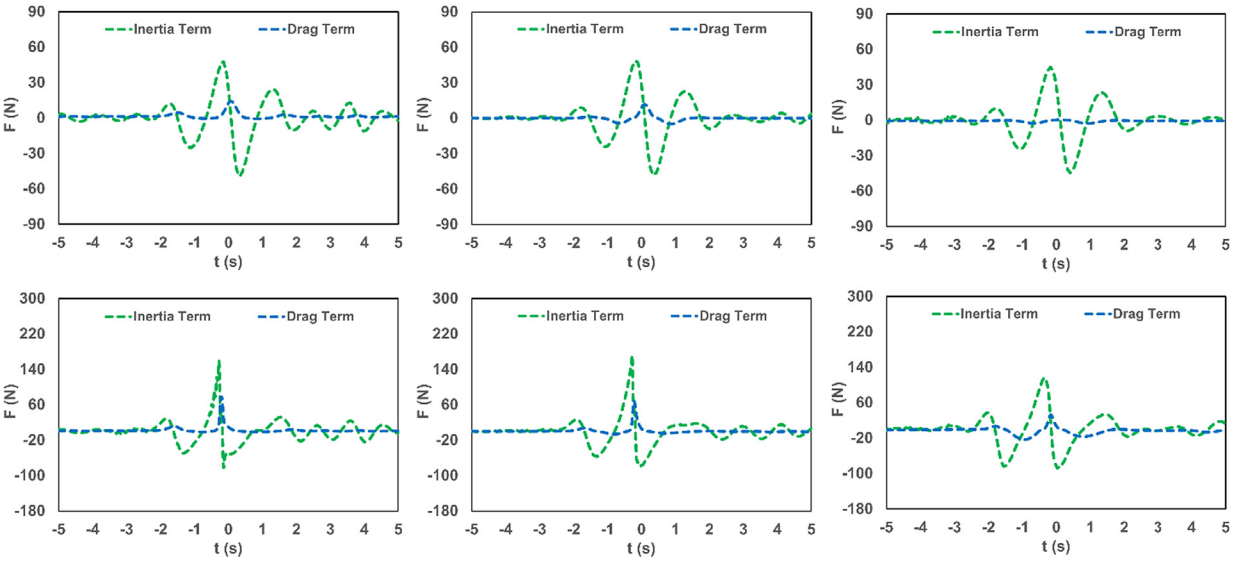

FIG. 20. Comparison between the inertia terms in the Morison equation and the drag terms in the Morison equation for crest focused waves. From top to bottom: original $\sum k_i a_i$ and largest $\sum k_i a_i$. From left to right: following sheared current case, no current case, and opposing sheared current case.

force in a 0° focused wave would be expected at around $-0.25\,T_p$ whereas this is observed at around $-0.1\,T_p$ for small amplitude waves and $-0.2\,T_p$ for steep breaking waves. Similarly, the maximum force for a 90° focused wave would be expected to occur at the focal time ($0\,T_p$) yet values closer to $0.2\,T_p$ are recorded. This problem becomes complex as we increase amplitude due to nonlinear dispersive effects along with the effect of bound harmonics on the kinematics and is further complicated by the presence of wave breaking. This is demonstrated in Fig. 17 showing the force time-history for the 90° focused wave cases in opposing current as we increase amplitude. A moderate shift in the time of maximum force is observed with amplitude until the largest case, which is probably due to wave nonlinearity. For the largest wave case where there is breaking, the wave prior to the largest crest predicted by linear theory breaks and introduces a large slamming force, explaining the $-1.05\,T_p$ time recorded for the maximum force in Table II. However, the positive peak horizontal force occurs during a period of a positive slope in the time histories of the free-surface elevation at the front face of the cylinder for almost all cases, which corresponds to a time associated with large particle accelerations. This is broadly consistent with the NewForce approach[70] and the findings in the experimental investigation of near-breaking and spilling breaking wave forces on a cylinder,[71] yet the precise times are more difficult to predict due to the highly nonlinear waves and the presence of wave breaking. Wave breaking and the associated slamming, energy redistribution, and dissipation can affect this significantly (as indicated in Fig. 17), and it is noted that for the largest $\sum k_i a_i$ for the 270° focused wave without current, the maximum force occurs closer to the time maximum elevation where wave breaking and slamming forces dominate. The complex relationship observed for which phase introduces the largest force and when this force occurs, particularly in breaking waves, warrants further exploration. It may be required to test a wide range of focused wave phases and relative positions in order to truly identify the peak design loads.

In Fig. 18, the simulation snapshots of the horizontal velocity field at the instant listed in Table II are shown (only the largest $\sum k_i a_i$). It demonstrates the effectiveness of using the SPH method for numerical modeling of wave–current–structure interaction with high nonlinearity and wave breaking. The results are all for a fixed depth with intermediate-depth waves. The force magnification by breaking over non-breaking waves has been shown experimentally (in regular waves without currents) to be dependent on the depth parameter kd with magnification varying from about × 3 in shallow water to negligible in deep water waves,[72] and the effect of depth parameter will be studied in further work.

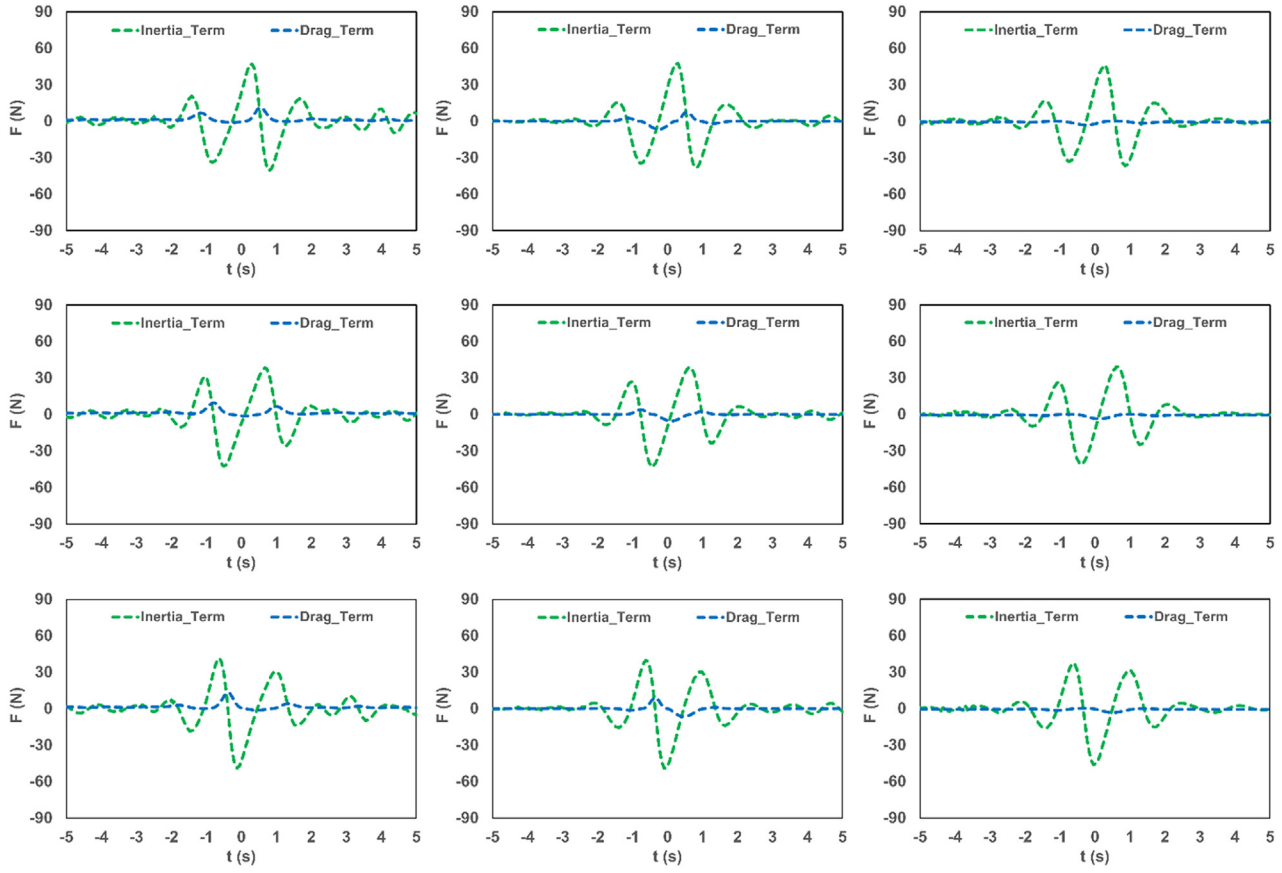

FIG. 21. Comparison between the inertia terms in the Morison equation and the drag terms in the Morison equation for other focused waves. From top to bottom: focused wave groups generated with phase shifts of 90°, 180°, and 270°. From left to right: following sheared current case, no current case, and opposing sheared current case.

C. Comparison with the Morison equation

In the present study, the hydrodynamic force on the cylinder is dominated by inertial effects with limited effect of diffraction with $D/L_p \approx 0.077$ (D is cylinder diameter, and L_p is peak wavelength).[73] Therefore, the Morison equation[74] can be used to reconstruct the time histories of horizontal force based on inertia term and drag term for most of the cases in Sec. V B. The inertia coefficient C_M and drag coefficient C_D in the Morison equation are computed and shown in Tables III and IV to investigate the contribution of the inertia term and the drag term on the horizontal force on the cylinder. In the Morison equation, the horizontal force dF on a strip of length dz of a rigid vertical circular cylinder is given by

$$\mathrm{d}F = \rho\frac{\pi D^2}{4}C_M a_x \mathrm{d}z + \frac{\rho}{2}C_D D v_x|v_x|\mathrm{d}z, \tag{23}$$

where ρ is the density of the water, D is the diameter of the cylinder, and v_x and a_x are the horizontal undisturbed fluid velocity and acceleration at the midpoint of the strip. To calculate the best values of C_M and C_D for the Morison equation to represent the time histories of horizontal force computed directly in the SPH model, an optimization approach is implemented varying C_M and C_D simultaneously to minimize the following objective function [time history of horizontal force on the cylinder, e.g., from $t = t_1$ $(i = 1)$ to $t = t_n$ $(i = n)$]:

$$Objective = \sum_{i=1}^{n}\left(F(t_i)^{SPH} - F(t_i)^{ME}\right)^2, \tag{24}$$

where $F(t_i)^{SPH}$ is the time history of horizontal force computed in the SPH model (subtracting the small mean force), and $F(t_i)^{ME}$ is the time history of horizontal force computed in the Morison equation, based on a 10 s time duration from −5 to 5 s. The computed optimized values of C_M and C_D are listed in Tables III and IV, respectively. For focused waves on a following sheared current, focused waves only, and focused waves on an opposing sheared current, the original $\sum k_i a_i$ is 0.143, 0.153, and 0.172, while the largest $\sum k_i a_i$ is 0.3, 0.35, and 0.45, respectively.

According to Tables III and IV, the values of C_M are close to 2, while the values of C_D vary from 0.41 to 2.27. The inertia term is dominant in the present study, and the effect of the drag term is relatively small so that the values of C_D are less important to determine the total force. It is consistent with the investigation of the variability of the

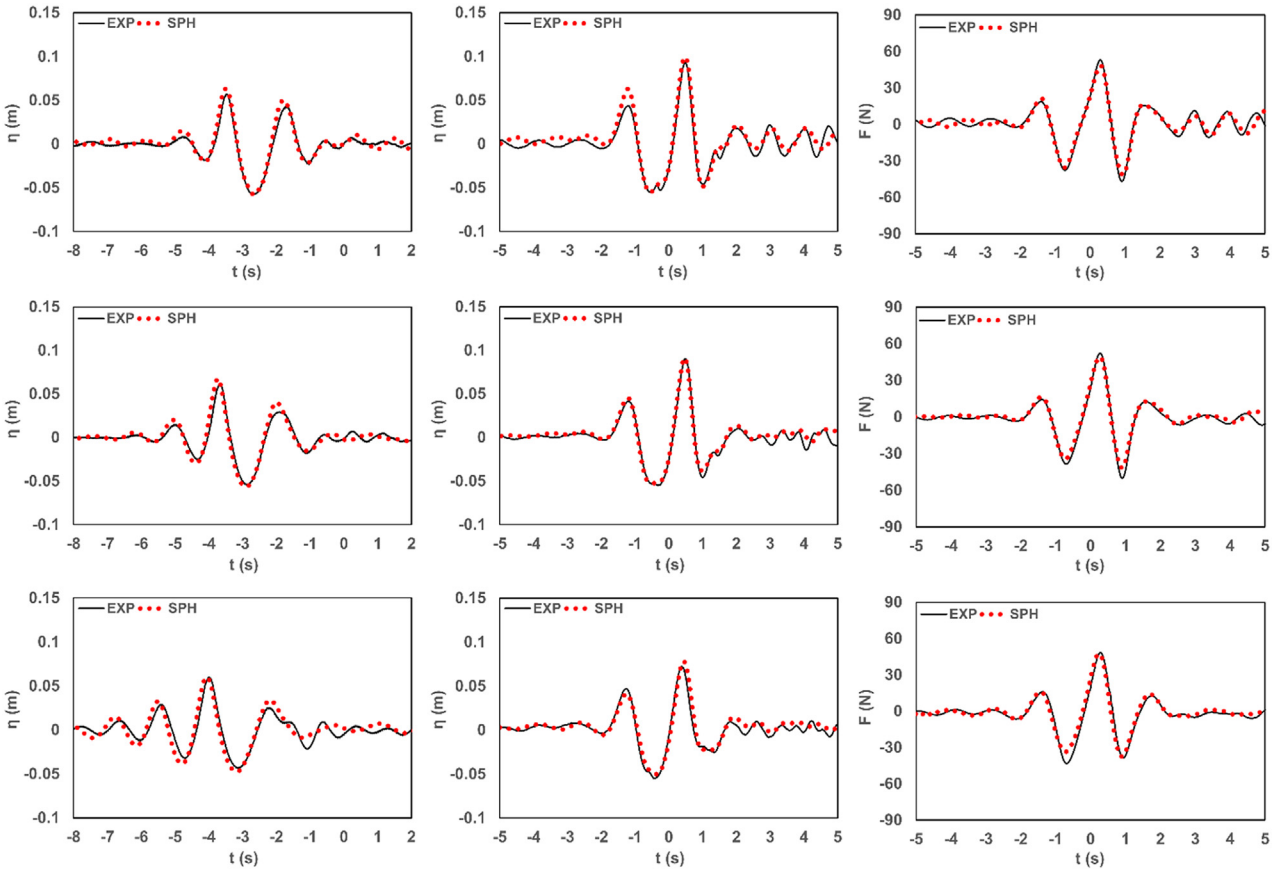

FIG. 22. Comparison between the numerical results in the SPH numerical model and measurements in the experiments for focused waves generating with the phase shift 90°. From top to bottom: following sheared current case, no current case, and opposing sheared current case. From left to right: surface elevation at $x = -4.7$ m, surface elevation at $x = -0.02$ m, and horizontal force on the cylinder.

inertia and drag coefficients considering the Morison wave force on a fixed vertical cylinder due to irregular waves in Ref. 75. In their study, irregular wave tests were also inertia dominated that it was found that there is a high variability in the constant drag coefficient compared to the inertia coefficient (close to 2) and that the precise value has a negligible effect on the wave force prediction owing to the predominance of the inertia term. The values of C_M are close to the potential flow value of 2, and small differences here are due to viscous effects.[76]

The time histories of horizontal force using the Morison equation with the values of C_M and C_D in Tables III and IV are compared with the time histories of horizontal force computed in the SPH model (subtracting the small mean force) for focused wave groups with the phase shifts of 0° at the original $\sum k_i a_i$ and the largest $\sum k_i a_i$ (the breaking wave cases) in Fig. 19. It is noted that the Morison equation is not recommended to predict the horizontal force due to breaking waves due to slamming as indicated in Fig. 18. The reason for the observed discrepancy in cases at the largest $\sum k_i a_i$ in Fig. 19 is likely due to the slamming. The inertia terms and drag terms for these cases are compared in Fig. 20. It is noted that the drag-like term becomes more important in breaking wave cases.

For focused wave groups generated with phase shifts of 90°, 180°, and 270° for waves on a following sheared current, waves only, and waves on an opposing sheared current at the original $\sum k_i a_i$, the inertia terms and drag terms for these cases are compared in Fig. 21. It is indicated that the wave phase plays a less important role in determining the contribution of the inertia term and the drag term in the present study as the effect of drag term is small at the original $\sum k_i a_i$.

VI. CONCLUSIONS

Prediction of loadings on substructures of ORE systems in complex and extreme events of combined waves and sheared currents is of great significance for practical applications in offshore renewable energy. Numerical modeling of interactions of focused waves and sheared currents with a vertical cylinder using SPH-based DualSPHysics code has been introduced in the present study. To generate the conditions in the SPH numerical wave–current flume, open boundaries and a modified damping zone are implemented as in Ref. 32. The time histories of the surface elevation and flow kinematics used as boundary conditions at the inlet of the SPH numerical model are obtained using the Buldakov *et al.* model with an iterative wave focusing methodology to replicate the wave conditions and wave–current conditions generated in the physical flume. Additionally, a relatively long distance between the wavemaker and the cylinder in the

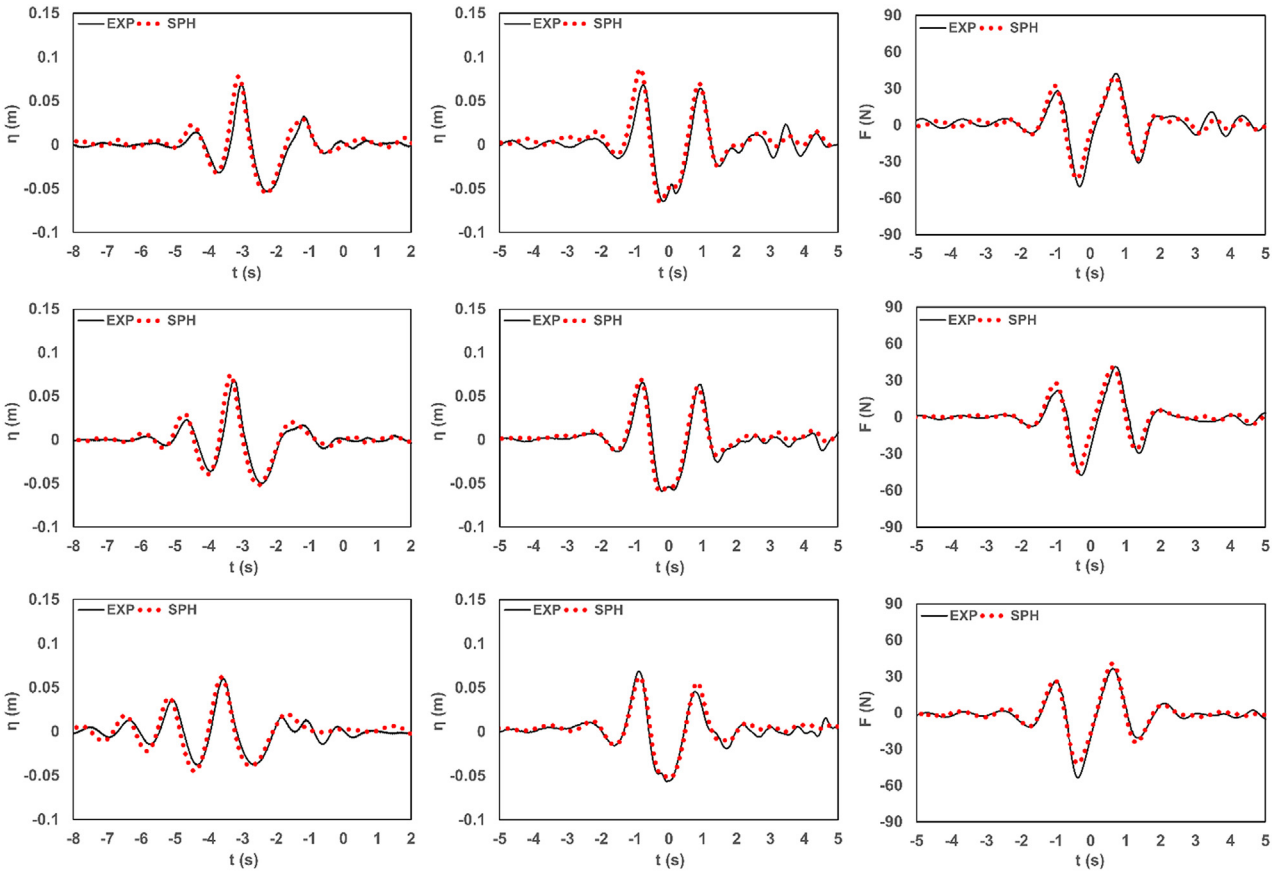

FIG. 23. Comparison between the numerical results in the SPH numerical model and measurements in the experiments for focused waves generating with the phase shift 180°. From top to bottom: following sheared current case, no current case, and opposing sheared current case. From left to right: surface elevation at $x = -4.7$ m, surface elevation at $x = -0.02$ m, and horizontal force on the cylinder.

physical flume is not required for the distance between the inlet and the cylinder in the SPH numerical model.

The numerical results from the SPH wave–current flume are validated with the Buldakov *et al.* model for surface elevation and velocity profile, demonstrating the accuracy of the method used to generate focused waves on different flow conditions (focused waves on a following sheared current, focused waves only, and focused waves on an opposing sheared current). Agreement between the numerical results from the SPH wave–current flume and experimental measurements for surface elevations and horizontal force on the cylinder is achieved, demonstrating the model's capability in the present study for modeling wave–current–structure interactions. Four phase repeats are used in the SPH model to understand the harmonic structure and extract the harmonic components of the surface elevation at the front face of the cylinder and associated loading on the cylinder. Harmonic components and amplitude spectra from harmonic analysis based on the numerical results and the experimental measurements show an overall good agreement. At the same time, a satisfactory computational performance is gained for 3D simulations by only using a laptop GPU, which is of great importance for practical applications in engineering.

The SPH-based numerical flume is well suited for modeling highly nonlinear fluid–structure interaction problems including wave breaking, and the peak forces on the cylinder in steep waves on sheared currents were investigated by increasing the wave amplitudes up to the breaking limit. Among the four focused wave groups with the phase shifts of 0°, 90°, 180°, and 270°, it was found that the maximum positive peak horizontal force on the cylinder is obtained in focused waves generated with phase shift 270° for two flow conditions (focused waves only and focused waves on an opposing sheared current), and with phase shift 0° for one flow condition (focused waves on a following sheared current). This is counter-intuitive to what we would expect from the linear theory, and the relationship between peak force and wave phase, along with when the peak force occurs, is found to be complex and warrants further study. An optimization approach was applied to calculate the inertia coefficient C_M and drag coefficient C_D in the Morison equation using kinematics from the SPH model. The comparisons indicate that the inertia effect is dominant and the effect of drag effect is relatively small in the present study. However, slamming is shown to be important for breaking wave cases, and the Morison equation is shown not to be able to capture the peak loads for these cases.

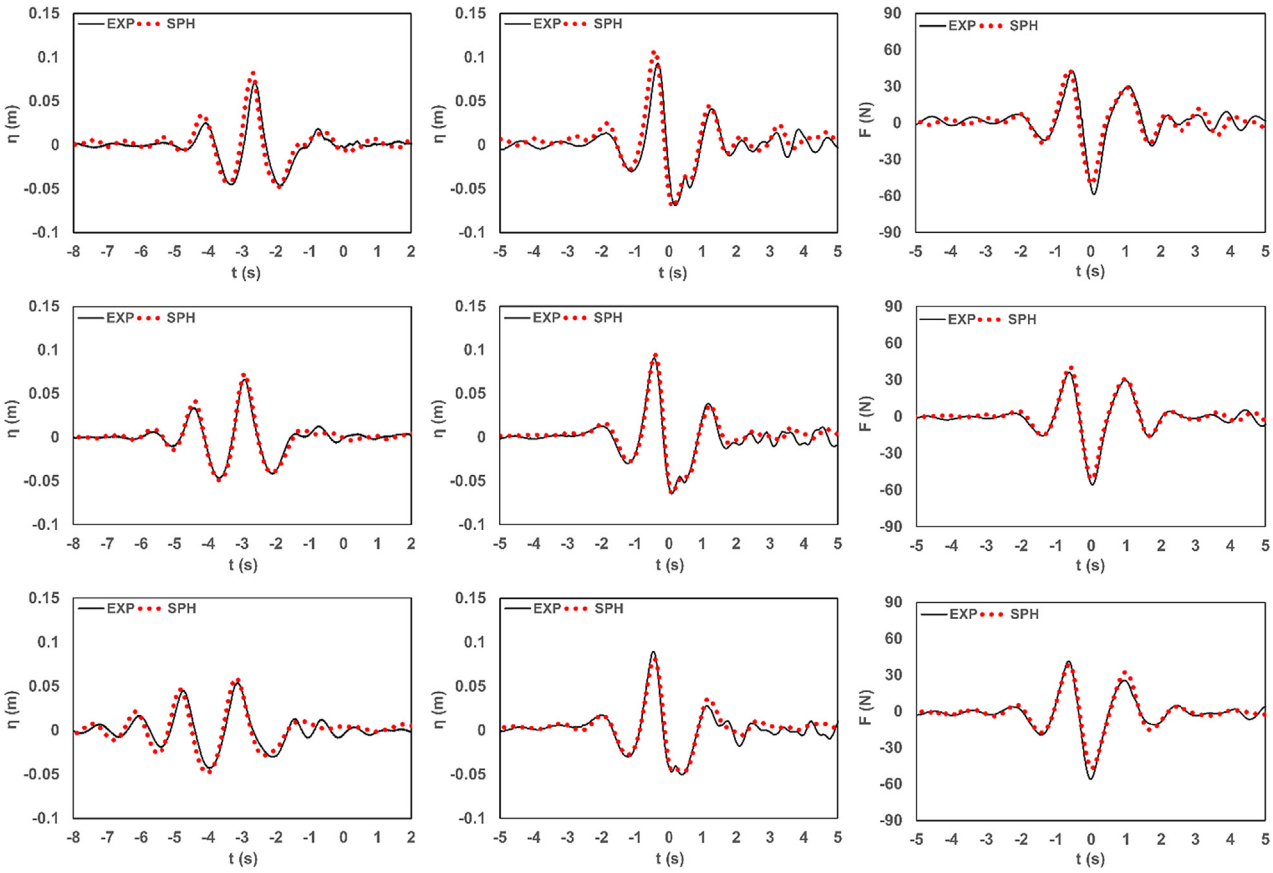

FIG. 24. Comparison between the numerical results in the SPH numerical model and measurements in the experiments for focused waves generating with the phase shift 270°. From top to bottom: following sheared current case, no current case, and opposing sheared current case. From left to right: surface elevation at $x = -4.7$ m, surface elevation at $x = -0.02$ m, and horizontal force on the cylinder.

ACKNOWLEDGMENTS

The authors would like to acknowledge funding for this project from the School of Engineering at the University of Manchester. S. Draycott acknowledges the Dame Kathleen Ollerenshaw Fellowship.

AUTHOR DECLARATIONS

Conflict of Interest

The authors have no conflicts to disclose.

Author Contributions

Yong Yang: Conceptualization (equal); Formal analysis (lead); Investigation (equal); Methodology (equal); Software (equal); Validation (lead); Writing – original draft (lead); Writing – review & editing (equal). **Peter Kenneth Stansby:** Conceptualization (equal); Methodology (equal); Resources (equal); Software (equal); Supervision (equal); Writing – review & editing (equal). **Benedict Rogers:** Conceptualization (equal); Methodology (equal); Resources (equal); Software (equal); Supervision (equal); Writing – review & editing (equal). **Eugeny Buldakov:** Conceptualization (equal); Methodology (equal); Resources (equal); Writing – review & editing (equal). **Dimitris Stagonas:** Conceptualization (equal); Methodology (equal); Resources (equal); Writing – review & editing (equal). **Samuel Draycott:** Conceptualization (equal); Funding acquisition (equal); Methodology (equal); Resources (equal); Supervision (equal); Writing – review & editing (equal).

DATA AVAILABILITY

The data that support the findings of this study are available within the article.

APPENDIX: FOCUSED WAVE GROUPS GENERATING WITH OTHER THREE PHASE SHIFTS

Four focused wave groups generating with the phase shifts of 0°, 90°, 180°, and 270° are required for the harmonic separation. Here, the measured numerical results of the surface elevations at the AMP and at the front face of the cylinder close to the FP and the horizontal forces on the cylinder are compared with the experiments for focused waves generating with the phase shift 90°, focused waves generating with the phase shift 180° and focused waves generating with the phase shift 270° on different flow conditions (following sheared current case, no current case, and opposing sheared current case) and are given in Figs. 22–24, respectively.

REFERENCES

[1]I. G. Jonsson, C. Skougaard, and J. D. Wang, "Interaction between waves and currents," in *Proceedings of the 12th Conference on Coastal Engineering* (ASCE, 1970), pp. 489–507.
[2]I. G. Jonsson, "Wave-current interactions," in *The Sea, Ocean Engineering Science*, edited by B. Le Méhauté and D. M. Hanes (Wiley, New York, 1990), pp. 65–120.
[3]J. M. Smith, "One-dimensional wave-current interaction," Technical Report No. 9, U.S. Army Engineer Waterways Experiment Station, Coastal Engineering Research Center Engineer Research and Development Center Vicksburg MS Coastal Hydraulics Lab (1997).
[4]P. Lin and C. W. Li, "Wave-current interaction with a vertical square cylinder," Ocean Eng. **30**, 855–876 (2003).
[5]Y. Jian, J. Zhan, and Q. Zhu, "Short crested wave-current forces around a large vertical circular cylinder," Eur. J. Mech. B/Fluids **27**, 346–360 (2008).
[6]Y. Li and M. Lin, "Hydrodynamic coefficients induced by waves and currents for submerged circular cylinder," Procedia Eng. **4**, 253–261 (2010).
[7]H. Xiao, W. Huang, J. Tao, and C. Liu, "Numerical modelling of wave-current forces acting on horizontal cylinder of marine structures by VOF method," Ocean Eng. **67**, 58–67 (2013).
[8]Z. Yang, B. Huang, A. Kang, B. Zhu, J. Han, R. Yin, and X. Li, "Experimental study on the solitary wave-current interaction and the combined forces on a vertical cylinder," Ocean Eng. **236**, 109569 (2021).
[9]H. Santo, D. Stagonas, E. Buldakov, and P. H. Taylor, "Current blockage in sheared flow: Experiments and numerical modelling of regular waves and strongly sheared current through a spaced-frame structure," J. Fluid Struct. **70**, 374–389 (2017).
[10]H. Santo, P. H. Taylor, A. H. Day, E. Nixon, and Y. S. Choo, "Current blockage and extreme forces on a jacket model in focussed wave groups with current," J. Fluid Struct. **78**, 24–35 (2018).
[11]S. Draycott, A. Nambiar, B. Sellar, T. Davey, and V. Venugopal, "Assessing extreme loads on a tidal turbine using focused wave groups in energetic currents," Renewable Energy **135**, 1013–1024 (2019).
[12]D. Ning, L. Chen, H. Lin, Q. Zou, and B. Teng, "Interaction mechanisms among waves, currents and a submerged plate," Appl. Ocean Res. **91**, 101911 (2019).
[13]Y. Li, M. Cai, Y. Z. Law, S. Zhang, and H. Santo, "Wave-current-structure blockage: Development of one-way hydro-structural coupling for a jack-up platform in waves and current," Ocean Eng. **258**, 111824 (2022).
[14]C. J. Fitzgerald, P. H. Taylor, R. E. Taylor, J. Grice, and J. Zang, "Phase manipulation and the harmonic components of ringing forces on a surface-piercing column," Proc. R. Soc. London, Ser. A **470**, 20130847 (2014).
[15]M. Mohseni, P. T. Esperanca, and S. H. Sphaier, "Numerical study of wave run-up on a fixed and vertical surface-piercing cylinder subjected to regular, non-breaking waves using OpenFOAM," Appl. Ocean Res. **79**, 228–252 (2018).
[16]L. F. Chen, D. Stagonas, H. Santo, E. V. Buldakov, R. R. Simons, P. H. Taylor, and J. Zang, "Numerical modelling of interactions of waves and sheared currents with a surface piercing vertical cylinder," Coastal Eng. **145**, 65–83 (2019).
[17]X. Feng, P. H. Taylor, S. Dai, A. H. Day, R. H. J. Willden, and T. A. A. Adcock, "Experimental investigation of higher harmonic wave loads and moments on a vertical cylinder by a phase-manipulation method," Coastal Eng. **160**, 103747 (2020).
[18]A. Ghadirian, M. H. Vested, S. Carstensen, E. D. Christiensen, and H. Bredmose, "Wave-current interaction effects on waves and their loads on a vertical cylinder," Coastal Eng. **165**, 103832 (2021).
[19]S.-C. Jiang, W. Bai, and B. Yan, "Higher-order harmonic induced wave resonance for two side-by-side boxes in close proximity," Phys. Fluids **33**, 102113 (2021).
[20]D. Mj, M. L. McAllister, H. Bredmose, T. A. A. Adcock, and P. H. Taylor, "Harmonic structure of wave loads on a surface piercing column in directionally spread and unidirectional random seas," J. Ocean Eng. Mar. Energy **9**, 415–433 (2023).
[21]H. Chen, L. Qian, and D. Cao, "Harmonic structure of the nonlinear force on a fixed ship-shaped floating production, storage and offloading vessel under dispersive phase-focused wave groups," Phys. Fluids **35**, 042103 (2023).
[22]R. A. Gingold and J. J. Monaghan, "Smoothed particle hydrodynamics: Theory and application to non-spherical stars," Mon. Not. R. Astron. Soc. **181**, 375–389 (1977).
[23]L. B. Lucy, "A numerical approach to the testing of the fission hypothesis," Astron. J. **82**, 1013–1024 (1977).
[24]D. Violeau and B. D. Rogers, "Smoothed particle hydrodynamics (SPH) for free-surface flows: Past, present and future," J. Hydraul. Res. **54**, 1–26 (2016).
[25]H. Gotoh and A. Khayyer, "Current achievements and future perspectives for projection-based particle methods with applications in ocean engineering," J. Ocean Eng. Mar. Energy **2**, 251–278 (2016).
[26]Z.-B. Wang, R. Chen, H. Wang, Q. Liao, X. Zhu, and S.-Z. Li, "An overview of smoothed particle hydrodynamics for simulating multiphase flow," Appl. Math. Modell. **40**, 9625–9655 (2016).

[27]M. S. Shadloo, G. Oger, and D. Le Touzé, "Smoothed particle hydrodynamics method for fluid flows, towards industrial applications: Motivations, current state, and challenges," Comput. Fluids **136**, 11–34 (2016).
[28]T. Ye, D. Pan, C. Huang, and M. Liu, "Smoothed particle hydrodynamics (SPH) for complex fluid flows: Recent developments in methodology and applications," Phys. Fluids **31**, 011301 (2019).
[29]M. Luo, A. Khayyer, and P. Lin, "Particle methods in ocean and coastal engineering," Appl. Ocean Res. **114**, 102734 (2021).
[30]M. He, X. Gao, and W. Xu, "Numerical simulation of wave-current interaction using the SPH method," J. Hydrodyn. **30**, 535–538 (2018).
[31]X. Ni, W. Feng, S. Huang, Z. Hu, and Y. Liu, "An SPH wave-current flume using open boundary conditions," J. Hydrodyn. **32**, 536–547 (2020).
[32]Y. Yang, S. Draycott, P. K. Stansby, and B. D. Rogers, "A numerical flume for waves on variable sheared currents using smoothed particle hydrodynamics (SPH) with open boundaries," Appl. Ocean Res. **135**, 103527 (2023).
[33]Y. Shi, S. Li, H. Chen, M. He, and S. Shao, "Improved SPH simulation of spilled oil contained by flexible floating boom under wave-current coupling condition," J. Fluids Struct. **76**, 272–300 (2018).
[34]X. Liu, S. Li, Z. Ji, and Q. Wu, "SPH simulation of hydrodynamic responses for two novel types of silt curtain under combined wave-current conditions," Appl. Ocean Res. **117**, 102906 (2021).
[35]H. Wen, B. Ren, P. Dong, and Y. Wang, "A SPH numerical wave basin for modeling wave-structure interactions," Appl. Ocean Res. **59**, 366–377 (2016).
[36]S. J. Lind, P. K. Stansby, and B. D. Rogers, "Fixed and moored bodies in steep and breaking waves using SPH with the Froude-Krylov approximation," J. Ocean Eng. Mar. Energy **2**, 331–354 (2016).
[37]A. D. Chow, B. D. Rogers, S. J. Lind, and P. K. Stansby, "Numerical wave basin using incompressible smoothed particle hydrodynamics (ISPH) on a single GPU with vertical cylinder test cases," Comput. Fluids **179**, 543–562 (2019).
[38]J. M. Domínguez, G. Fourtakas, C. Altomare, R. B. Canelas, A. Tafuni, O. García-Feal, I. Martínez-Estévez, A. Mokos, R. Vacondio, A. J. C. Crespo, B. D. Rogers, P. K. Stansby, and M. Gómez-Gesteira, "DualSPHysics: From fluid dynamics to multiphysics problems," Comput. Part. Mech. **9**, 867–895 (2022).
[39]C. Altomare, J. M. Domínguez, A. J. C. Crespo, J. González-Cao, T. Suzuki, M. Gómez-Gesteira, and P. Troch, "Long-crested wave generation and absorption for SPH-based DualSPHysics model," Coastal Eng. **127**, 37–54 (2017).
[40]T. Verbrugghe, J. M. Domínguez, C. Altomare, A. Tafuni, R. Vacondio, P. Troch, and A. Kortenhaus, "Non-linear wave generation and absorption using open boundaries within DualSPHysics," Comput. Phys. Commun. **240**, 46–59 (2019).
[41]A. Tafuni, J. M. Domínguez, R. Vacondio, and A. J. C. Crespo, "A versatile algorithm for the treatment of open boundary conditions in smoothed particle hydrodynamics GPU models," Comput. Methods Appl. Mech. Eng. **342**, 604–624 (2018).
[42]S. Capasso, B. Tagliafierro, R. González-Avalos, I. Martínez-Estévez, J. M. Domínguez, C. Altomare, A. J. C. Crespo, and G. Viccione, "Numerical simulation of a moored wave-buoy in waves and current by smoothed particle hydrodynamics," in *Proceedings of the ASME 2023 42nd International Conference on Ocean, Offshore and Arctic Engineering* (OMAE, 2023).
[43]R. J. Rapp and W. K. Melville, "Laboratory measurements of deep-water breaking waves," Philos. Trans. R. Soc., A **331**, 735–800 (1990).
[44]J. Chaplin, "On frequency-focusing unidirectional waves," Int. J. Offshore Polar Eng. **6**, 131–137 (1996).
[45]A. Yao and C. H. Wu, "Incipient breaking of unsteady waves on sheared currents," Phys. Fluids **17**, 082104 (2005).
[46]C. Schmittner, S. Kosleck, and J. Hennig, "A phase-amplitude iteration scheme for the optimization of deterministic wave sequences," in *Proceedings of the ASME 2009 28th International Conference on Ocean, Offshore and Arctic Engineering* (OMAE, 2009).
[47]H. Fernández, V. Sriram, S. Schimmels, and H. Oumeraci, "Extreme wave generation using self correcting method—Revisited," Coastal Eng. **93**, 15–31 (2014).
[48]D. Stagonas, E. Buldakov, and R. Simons, "Focusing unidirectional wave groups on finite water depth with and without currents," in *Proceedings of the 34th International Coastal Engineering Conference* (ICCE, 2014).
[49]E. Buldakov, D. Stagonas, and R. Simons, "Extreme wave groups in a wave flume: Controlled generation and breaking onset," Coastal Eng. **128**, 75–83 (2017).
[50]D. Stagonas, E. Buldakov, and R. Simons, "Experimental generation of focusing wave groups on following and adverse-sheared currents in a wave-current flume," J. Hydraul. Eng. **144**, 04018016 (2018).
[51]D. Stagonas, P. Higuera, and E. Buldakov, "Simulating breaking focused waves in CFD: Methodology for controlled generation of first and second order," J. Waterw. Port, Coastal Ocean Eng. **144**, 06017005 (2018).
[52]E. V. Buldakov, P. H. Taylor, and R. E. Taylor, "New asymptotic description of nonlinear water waves in Lagrangian coordinates," J. Fluid Mech. **562**, 431–444 (2006).
[53]E. Buldakov, D. Stagonas, and R. Simons, "Lagrangian numerical wave-current flume," in 30th International Workshop on Water Waves and Floating Bodies (2015).
[54]M. Antuono, A. Colagrossi, S. Marrone, and D. Molteni, "Free-surface flows solved by means of SPH schemes with numerical diffusive terms," Comput. Phys. Commun. **181**, 532–549 (2010).
[55]G. Fourtakas, J. M. Domínguez, R. Vacondio, and B. D. Rogers, "Local uniform stencil (LUST) boundary condition for arbitrary 3-D boundaries in parallel smoothed particle hydrodynamics (SPH) models," Comput. Fluids **190**, 346–361 (2019).
[56]J. J. Monaghan, "Smoothed particle hydrodynamics," Annu. Rev. Astron. Astrophys. **30**, 543–574 (1992).
[57]H. Wendland, "Piecewise polynomial, positive definite and compactly supported radial functions of minimal degree," Adv. Comput. Math. **4**, 389–396 (1995).
[58]M. Antuono, A. Colagrossi, and S. Marrone, "Numerical diffusive terms in weakly-compressible SPH schemes," Comput. Phys. Commun. **183**, 2570–2580 (2012).
[59]P. Sun, F. Ming, and A. Zhang, "Numerical simulation of interactions between free surface and rigid body using a robust SPH method," Ocean Eng. **98**, 32–49 (2015).
[60]A. J. C. Crespo, M. Gómez-Gesteira, and R. A. Dalrymple, "Boundary conditions generated by dynamic particles in SPH methods," Comput. Mater. Continua **5**, 173–184 (2007).
[61]A. English, J. M. Domínguez, R. Vacondio, A. J. C. Crespo, P. K. Stansby, S. J. Lind, L. Chiapponi, and M. Gómez-Gesteira, "Modified dynamic boundary conditions (mDBC) for general-purpose smoothed particle hydrodynamics (SPH): Application to tank sloshing, dam break and fish pass problems," Comput. Part. Mech. **9**, 1–15 (2022).
[62]X. Ni, W. Feng, S. Huang, Y. Zhang, and X. Feng, "A SPH numerical wave flume with non-reflective open boundary conditions," Ocean Eng. **163**, 483–501 (2018).
[63]J.-S. Zhang, Y. Zhang, D.-S. Jeng, P. L.-F. Liu, and C. Zhang, "Numerical simulation of wave-current interaction using a RANS solver," Ocean Eng. **75**, 157–164 (2014).
[64]A. G. L. Borthwick, A. C. Hunt, T. Feng, P. H. Taylor, and P. K. Stansby, "Flow kinematics of focused wave groups on a plane beach in the U.K. Coastal Research Facility," Coastal Eng. **53**, 1033–1044 (2006).
[65]J. Orszaghova, P. H. Taylor, A. G. L. Borthwick, and A. C. Raby, "Importance of second-order wave generation for focused wave group run-up and overtopping," Coastal Eng. **94**, 63–79 (2014).
[66]A. Khayyer, Y. Shimizu, T. Gotoh, and H. Gotoh, "Enhanced resolution of the continuity equation in explicit weakly compressible SPH simulations of incompressible free-surface fluid flows," Appl. Math. Modell. **116**, 84–121 (2023).
[67]P. N. Sun, C. Pilloton, M. Antuono, and A. Colagrossi, "Inclusion of an acoustic damper term in weakly-compressible SPH models," J. Comput. Phys. **483**, 112056 (2023).
[68]D. D. Meringolo, A. Colagrossi, S. Marrone, and F. Aristodemo, "On the filtering of acoustic components in weakly-compressible SPH simulations," J. Fluids Struct. **70**, 1–23 (2017).
[69]O. G. Nwogu, "Interaction of finite-amplitude waves with vertically sheared current fields," J. Fluid Mech. **627**, 179–213 (2009).
[70]S. Schløer, H. Bredmose, and A. Ghadirian, "Analysis of experimental data: The average shape of extreme wave forces on monopile foundations and the NewForce model," Energy Procedia **137**, 223–237 (2017).

[71]J. M. Esandi, E. Buldakov, R. Simons, and D. Stagonas, "An experimental study on wave forces on a vertical cylinder due to spilling breaking and near-breaking wave groups," Coastal Eng. **162**, 103778 (2020).
[72]P. K. Stansby, L. C. Devaney, and T. J. Stallard, "Breaking wave loads on monopiles for offshore wind turbines and estimation of extreme overturning moment," IET Renewable Power Gener. **7**, 514–520 (2013).
[73]S. K. Chakrabarti, *Handbook of Offshore Engineering* (Elsevier, 2005).
[74]J. R. Morison, M. P. O'Brien, J. W. Johnson, and S. A. Schaaf, "The force exerted by surface waves on piles," J. Pet. Technol. **2**, 149–154 (1950).
[75]K. Raed and C. G. Soares, "Variability effect of the drag and inertia coefficients on the Morison wave force acting on a fixed vertical cylinder in irregular waves," Ocean Eng. **159**, 66–75 (2018).
[76]T. Sarpkaya, "Force on a circular cylinder in viscous oscillatory flow at low Keulegan-Carpenter numbers," J. Fluid Mech. **165**, 61–71 (1986).